

Multiscale methods for mechanical science of complex materials: Bridging from quantum to stochastic multiresolution continuum

Wing Kam Liu^{1,*}, Dong Qian², Stefano Gonella¹, Shaofan Li³, Wei Chen¹
and Shardool Chirputkar²

¹*Department of Mechanical Engineering, Northwestern University, 2145 Sheridan Road,
Evanston, IL 60208-3111, U.S.A.*

²*Department of Mechanical Engineering, University of Cincinnati, Cincinnati, OH 45221-0072, U.S.A.*

³*Department of Civil and Environmental Engineering, University of California, Berkeley, CA 94729, U.S.A.*

SUMMARY

Recent development in the multiscale method based on the bridging scale concept is presented with an emphasis on complex material systems. The bridging scale method (BSM) was originally proposed by Wagner and Liu (*J. Comput. Phys.* 2003; **190**:249–274) as an effective way of treating the interface in coupled atomistic/continuum simulation. Since its publication, the BSM has become a very useful paradigm that has been applied to solve a host of problems in mechanical sciences of complex material systems. In this paper, we present a review on the recent developments. We first describe the application of BSM to the coupled atomistic/continuum simulation of dynamic fracture. The important extensions within the framework of space–time method and multiscale non-equilibrium molecular dynamics are then presented. We then focus on the multiresolution continuum theory that inherits the BSM concept in the analysis of heterogeneous material structures. Recent work of incorporating statistical factors into this model based on the concurrent nested homogenization of randomness of the material structures is highlighted. Finally, we present the use of the bridging scale concept in resolving the electron-mechanical coupling mechanism. The robustness of the BSM is demonstrated through many benchmark problems and application examples. Copyright © 2010 John Wiley & Sons, Ltd.

Received 3 August 2009; Revised 15 March 2010; Accepted 15 March 2010

KEY WORDS: bridging scale method; multiresolution continuum; coupled atomistic/continuum simulation; multiscale non-equilibrium method; quantum-mechanical coupling; virtual atom-cluster

*Correspondence to: Wing Kam Liu, Department of Mechanical Engineering, Northwestern University, 2145 Sheridan Road, Evanston, IL 60208-3111, U.S.A.

†E-mail: w-liu@northwestern.edu

Contract/grant sponsor: National Science Foundation; contract/grant numbers: CMMI-0823327, CMMI-0600583, CMMI-0700107, CMMI-0522662, CMS-0239130

Contract/grant sponsor: Army Research Lab; contract/grant number: ONR/DAPRA D3D

Contract/grant sponsor: World Class University; contract/grant number: R33-10079

1. INTRODUCTION

The field of multiscale design for the new generation of material systems is rapidly advancing. In particular, there is a continuing interest in studying the structure–property relations in engineering materials with constituents that span over multiple spatial scales. For these type of material systems, the direct use of simulation tools such as quantum mechanics [1], molecular dynamics [2], or continuum methods [3] is facing difficulties due to the limited range of scales that each model is capable of addressing. In contrast, the hierarchical structure of the material often involves components that are defined at the micro- or even nano-meter length scales [4–8].

To circumvent the computational expense issues, models based on homogenization theory have been developed. The basic idea is to derive homogenized properties by studying the essential features of the underlying microstructures [9]. A so-called representative volume element (RVE) is extracted based on the periodicity of the material structure. The equivalent continuum models are then developed using a hierarchical approach. In a typical setting, one starts with the finest scale and proceeds to coarse grain the material behavior at that scale to arrive at the next upper coarse scale. Through successive up-scaling, the final continuum model is obtained with an embedded representation of fine scale effects such as those due to dislocation, void nucleation and growth, grain boundary formation and migration, etc.

While the periodicity assumption has been used as an important condition for deriving the RVE, it is not always valid when there is localized deformation within the microstructure or new interfaces are forming due to phase transformation. In these cases, the RVE-based homogenization approach may result in large discrepancies. As such, the important material behaviors that are due to the inherent inhomogeneity cannot be fully accounted for. This leads to further errors in predicting important material properties and performance.

In light of the difficulties associated with the use of the homogenization theory alone, a number of hybrid approaches that combine direct numerical simulations (DNS) and homogenization theory have been developed. Typically, DNS will be applied in the regions of the domain where homogenization gives poor predictions. Representative examples of this approach include the use of multiscale Hamiltonian [10], multigrid method [11], Green's function [12], quasi-continuum (QC) model [13], generalized Langevin equation [14–16], Arlequin coupling method [17, 18], the bridge-domain method [19, 20] and many others. Owing to limited scope, we will not present detailed review on each of the methods. In many of these methods, the atomistic simulation is limited to particular regions of interest and the coupled analysis is limited to nanoscale structures and materials (e.g. carbon nanotubes (CNT)) [21, 22].

An alternative approach to consider the heterogeneous material effect is to extend the conventional continuum mechanics theory. A classic example of this ‘top-down’ approach is the incorporation of the geometric necessary dislocation effects in the strain gradient theory [23, 24] based on experimental observations [25]. Because of the intrinsic length scale that is part of the material model parameter, numerical simulation using strain gradient model does not suffer from the mesh dependency problem in modeling shear bands and fractures that arises with the use of classical plasticity models. Such a length scale was also incorporated in the bridging scale method (BSM) approach developed by Kadowaki and Liu [26] based on the micromorphic continuum theory [27]. While the original work was targeted at modeling localized deformation in granular materials, further extensions to a three-scale decomposition model have been made in McVeigh *et al.* [28] in modeling high-strength steel. More recently, a stochastic multiscale modeling approach [29–34] has been established.

The main objective of this paper is to review the BSM and its application to the analysis of nanostructured and heterogeneous materials. In addition, a general multiscale theory for heterogeneous materials, called multiresolution continuum theory (MRCT), has been recently proposed by Liu and coworkers [35–38] as a complement to the BSM. We will highlight some of the recent new development of this theory for multiscale material design, including the statistical multiresolution continuum analysis. The MRCT is based on concurrent nested statistical averaging homogenization of the fine scales within a single mesh discretization, and it involves scale coupling modeled through the introduction of additional degrees of freedom. This theory eliminates the need of wave elimination techniques that are characteristic of the BSM. Another major new development is the formulation of the bridging scale concept within the space–time framework and application of the BSM to the study of non-equilibrium phenomena. Recent developments in these two aspects are also presented. The remainder of the paper is organized as follows: a review on the BSM is first presented with a historic account of the development. We then proceed to discuss the application of this method for modeling material failure. After presenting the bridging scale treatment within the space–time framework and its extension to the study of non-equilibrium phenomena and heterogeneous material design, we focus on the MRCT. Our study based on statistical multiresolution continuum analysis is highlighted as a new direction of this approach. Finally, coupled electron-mechanical analysis based on the BSM is discussed. Conclusions are made based on a summary of the state-of-the-art development and future directions.

2. AN OVERVIEW OF THE INTERFACE TREATMENT IN COUPLED ATOMISTIC/CONTINUUM SIMULATION

2.1. Governing equations

We consider a system of atoms that are governed by the Lagrangian equations [2]

$$\frac{d}{dt} \frac{\partial L}{\partial \dot{\mathbf{r}}_i} - \frac{\partial L}{\partial \mathbf{r}_i} = 0, \quad i = 1, 2, \dots, N \quad (1)$$

in which, $\mathbf{r}_i = (x_i, y_i, z_i)$ is the position vector of atom i , and N is the total number of simulated atoms. The system's Lagrangian acquires the form:

$$L = \sum_{i=1}^N \frac{m_i \dot{\mathbf{r}}_i^2}{2} - U(\mathbf{r}_1, \mathbf{r}_2, \dots, \mathbf{r}_N) \quad (2)$$

in which the two terms on the right-hand side give the system's kinetic and potential energy, respectively. Combining Equations (1) and (2) yields the equations of motion in the Newtonian form,

$$m_i \ddot{\mathbf{r}}_i = - \frac{\partial U(\mathbf{r}_1, \mathbf{r}_2, \dots, \mathbf{r}_N)}{\partial \mathbf{r}_i} \equiv \mathbf{F}_i, \quad i = 1, 2, \dots, N \quad (3)$$

The force \mathbf{F}_i is usually referred to as the *internal force*, i.e. the force exerted on atom i due to specifics of the environment it is exposed to. Equation (3) is solved for a given set of initial conditions to get trajectories of the atomic motion in the simulated system.

2.2. A brief historic account on interface treatment

As mentioned in the introduction, obtaining direct solution to Equation (3) is what we referred to as the DNS approach. Performing DNS for complex material system is prohibitively expensive. An alternative is then to develop hybrid approaches that combine DNS with a coarse-grained approach such as finite element method (FEM). In this implementation, a key issue is the treatment of the numerical interface due to the presence of different simulation techniques used in different domains. Earlier implementation of coupling finite element (FE) with molecular dynamics and statics is featured by an FEM mesh refinement process to the atomic resolution at this interface. Correspondingly, the nodal and atomistic DOFs are enforced to be the same at the interface, i.e.

$$\mathbf{x}_\alpha = \sum_{I=1}^{NP} \mathbf{N}_{I\alpha} \mathbf{d}_I = \mathbf{d}_\alpha \quad (4)$$

where \mathbf{x}_α is the degree-of-freedom of the α th atom and $\mathbf{N}_{I\alpha}$ is the shape function defined at the I th FEM node and evaluated at the location of the α th atom. The terms \mathbf{d}_I and \mathbf{d}_α represent the nodal and atomic degrees of freedom, respectively. The last term is simply the nodal degree-of-freedom that corresponds to the α th atom. Although the summation in Equation (4) is performed over the total number of nodes NP , numerical implementation often involves a local sum due to the local support of the FEM shape function. This approach has been employed in the simulation of brittle fracture [39–41]. Another major class of method that adopts this approach is the QC method [42]. In the QC method, representative atoms are selected to be the nodes of FEM and full atomistic resolutions are employed in the regions that are governed by the fine scale physics such as defects, dislocations and fractures.

Holian and Ravelo [43] reported that the sound wave generated from the crack simulation using the direct handshake approach makes the prediction unreliable. To resolve this issue, they proposed to include a viscous damping term in the equation of motion. Compared with the original equation of motion (Equation (3)), the revised version is given as:

$$m_i \ddot{\mathbf{r}}_i = \mathbf{F}_i - \gamma \left(1 - \frac{T_0}{T} \right) m_i \dot{\mathbf{r}}_i, \quad i = 1, 2, \dots, N \quad (5)$$

Equation (5) can be implemented based on the Berendsen thermostat [44]. Here γ is the damping rate at zero temperature, T_0 is the temperature of the thermal bath and T is the instantaneous kinetic temperature. If Equation (5) is applied to all the atoms within the simulation, it has been shown that the nature of the crack could switch between brittle and ductile when different values of γ are used. Further extension of this method is presented in [5, 45] in which the viscous damping is only applied at the interface.

Based on the generalized Langevin method developed by Adelman and Doll [46, 47], Cai *et al.* [48] proposed an extension of this approach to couple the atomistic simulation to a linear elastic system. The goal is to eliminate the wave reflections arising at the numerical interface. In 1D version, the basic formulation of this method can be expressed as follows:

$$m_i \ddot{x}_i = -\frac{\partial U}{\partial x_i} + \int_0^t \sum_{j=1}^N \beta_{ij}(\tau) \dot{x}_j(t-\tau) d\tau + \sum_{j=1}^N \beta_{ij}(\tau) x_j(0) + R_i(t) \quad (6)$$

in which U is the system potential. Equation (6) degenerates to the case of pure atomistic simulation if the last three terms on the RHS of Equation (6) are neglected. The wave reflection is minimized

mainly through the second term on the right-hand side, which provides energy dissipation through viscous damping. The term β is called a time-history kernel: it represents the time-history effect of the atoms in the linear elastic region on the atoms in the simulation region. The third term denotes the effect due to the initial conditions. The last term mimics the energy exchange between the atomistic and elastic region due to the random thermal fluctuations. The computational implementation for Equation (6) can be regarded as a dynamic Green's function approach in that it seeks to provide the interfacial boundary conditions for the atomistic simulation by analytically solving the molecular dynamic equation under linear assumption. E and Huang [49] pointed out that the dynamic Green's function derived in [48] is expensive to compute due to its non-local nature in both space and time. As an alternative, they proposed to minimize the reflection of the wave at the interface R , which can be defined as the ratio between the incoming and outgoing waves. It was then expressed in terms of coefficients associated with the frequency ω and the wave number ξ , i.e.

$$R = R(\omega, \xi) \quad (7)$$

Analytical expressions for linear system were derived based on different orders of expansions in [49, 50]. The implementation of this interfacial treatment in the coupled atomistic/continuum simulation setting was demonstrated in [49, 50] in which it was shown that the artificial wave reflection can be minimized as expected.

3. THE BRIDGING SCALE APPROACH AND EXTENSIONS

3.1. Coarse-fine scale decomposition

While all the approaches outlined in the last section have had some success in designing a seamless interface, one problem that has not been directly addressed is the multiple spatial and temporal scales that generally arise from the mechanics or physics of the application. Motivated by this gap, the BSM was first developed by Wagner and Liu [51] to couple atomistic and continuum scales in the context of dynamic simulations. The main feature of BSM is its ability to handle high-frequency wave propagation in dynamic problems. It seamlessly eliminates the spurious numerical interface phenomena arising at the interfaces between scales that heavily affect other multiscale methods. One important characteristic of the method lies in the concurrent coupling between the scales, which means that the solutions of the two scales are assumed to exist *simultaneously* over the computational domain, and in a set of back and forth information exchanges between scales, even if the atomistic calculations are explicitly performed only inside a defined fine scale region. The fundamental idea of the method is to decompose the total displacement field $\mathbf{u}(\mathbf{x}, t)$ into a coarse scale and a fine scale contribution:

$$\mathbf{u}(\mathbf{x}, t) = \bar{\mathbf{u}}(\mathbf{x}, t) + \tilde{\mathbf{u}}(\mathbf{x}, t) \quad (8)$$

where $\bar{\mathbf{u}}(\mathbf{x}, t)$ is the coarse scale approximation of the solution, whereas $\tilde{\mathbf{u}}(\mathbf{x}, t)$ is called the enrichment, and is defined as the part of the total solution that has a vanishing projection onto the coarse scale. The coarse scale solution can be interpolated by basic FE or meshfree shape functions [52–54].

In an FE sense, the coarse scale solution can be expressed as $\bar{\mathbf{u}} = \mathbf{N}\mathbf{d}$, where \mathbf{d} is an array of coarse scale FE generalized degrees of freedom and \mathbf{N} is a matrix of shape functions evaluated at

the atomic locations. If $\bar{\mathbf{u}}_i$ represents the interpolation of the coarse scale FE solution \mathbf{d}_j at a fine scale nodal location \mathbf{x}_i through the shape function $\mathbf{N}_j(\mathbf{x}_i)$, the following holds:

$$\bar{\mathbf{u}}_i = \sum_{j=1}^{n_c} \mathbf{N}_j(\mathbf{x}_i) \mathbf{I}_{n_D} \mathbf{d}_j \quad (9)$$

where n_c defines the number of nodes in the coarse scale mesh and \mathbf{I}_{n_D} is an identity matrix of size n_D , with n_D denoting the number of degrees of freedom per node. The enrichment can be expanded as $\tilde{\mathbf{u}} = \mathbf{Q}\mathbf{q}$, where \mathbf{q} is an array of fine scale degrees of freedom obtained from atomistic calculations, and $\mathbf{Q} = \mathbf{I} - \mathbf{P}$, where \mathbf{P} is the projection operator that minimizes a selected error metric, typically the mass-weighted square of the fine scale solution, which is written as

$$J = \sum_{\alpha=1}^{n_f} m_{\alpha} \left(\mathbf{q}_{\alpha} - \sum_{i=1}^{n_c} \mathbf{N}_i(\mathbf{x}_{\alpha}) \mathbf{w}_i \right)^2 \quad (10)$$

where m_{α} is the mass of the α atom, n_f is the total number of atoms in the domain and \mathbf{w}_i are temporary coarse scale degrees of freedom. Wagner and Liu [51] showed that $\mathbf{P} = \mathbf{N}\mathbf{M}^{-1}\mathbf{N}^T\mathbf{M}_A$, where \mathbf{M}_A is a diagonal atomistic mass matrix and \mathbf{M} is the consistent FE mass matrix. It is important to point out that the method can also be used in a purely continuum mechanics scenario to couple simulations performed on meshes with different levels of refinement [26, 55]. In this case, the atomistic simulation is replaced by a second FE simulation performed using a fine mesh and the array \mathbf{q} contains the generalized nodal degrees of freedom of the fine scale FE solution.

3.2. Multiscale equations of motion

The coupled equations of motion for the two scales can be derived by constructing the Lagrangian L , defined as the difference between kinetic and potential energy:

$$L(\mathbf{u}, \dot{\mathbf{u}}) = K(\dot{\mathbf{u}}) - U(\mathbf{u}) \quad (11)$$

Following Lagrange's equations:

$$\begin{aligned} \frac{d}{dt} \left(\frac{\partial L}{\partial \dot{\mathbf{d}}} \right) - \frac{\partial L}{\partial \mathbf{d}} &= 0 \\ \frac{d}{dt} \left(\frac{\partial L}{\partial \dot{\mathbf{q}}} \right) - \frac{\partial L}{\partial \mathbf{q}} &= 0 \end{aligned} \quad (12)$$

The following coupled multiscale equations of motion are obtained for the homogeneous problem:

$$\mathbf{M}_A \ddot{\mathbf{q}} = \mathbf{f}(\mathbf{u}) \quad (13)$$

$$\mathbf{M} \ddot{\mathbf{d}} = \mathbf{N}^T \mathbf{f}(\mathbf{u}) \quad (14)$$

Equation (13) represents the standard atomistic equations of motion of a molecular dynamics (MD) system, where \mathbf{q} are the displacements of the atoms and \mathbf{f} the interatomic forces, calculated using a potential energy function. This equation is intended to be solved exclusively inside the designated MD region. On the contrary, Equation (14) that is the coarse scale equation of motion,

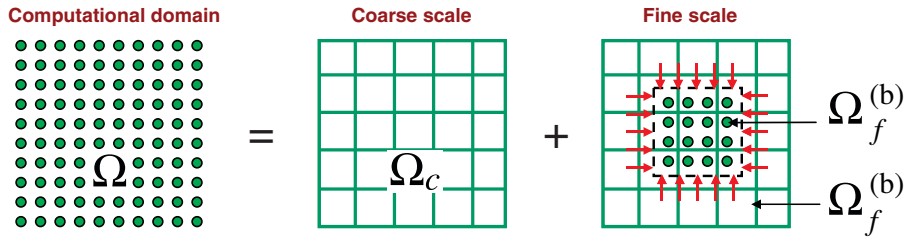


Figure 1. Schematic of bridging scales domain decomposition.

is solved with an FE procedure applied everywhere in the domain. The coupling between the two regions is established through the coarse scale internal force $\mathbf{N}^T \mathbf{f}(\mathbf{u})$. In the region where the MD solution exists, the FE nodal forces are then calculated by extrapolating the MD forces, which can therefore be thought of as providing the constitutive model for the FE formulation.

If we assume that the MD solution is available everywhere, then the coarse scale equation (Equation (14)) becomes redundant, as the total solution \mathbf{u} satisfies the same equation of motion of \mathbf{q} , i.e. $\mathbf{M}_A \ddot{\mathbf{u}} = \mathbf{f}(\mathbf{u})$, making Equation (13) sufficient to fully capture the fine scale behavior of the solid over the whole computational domain. The beneficial effects of the coupled scales are evident when the fine scale solution is calculated only within a small region of the domain (Figure 1). When the fine scale solution is eliminated from large portions of the domain, the MD displacements are not available everywhere anymore, and thus it is not possible to calculate the coarse scale solution through a simple projection of the MD displacements. In this case, the solution of the FE equations of motion ensures a continuous coarse scale displacement field. In this context, the domain is partitioned into two regions, $\Omega_f^{(a)}$ and $\Omega_f^{(b)}$. $\Omega_f^{(a)}$ represents the portion of the domain where a detailed description is needed. This is the case of regions where localized discontinuities, such as cracks, inclusions or other non-linearities, are present. This makes it insufficient for the coarse scale discretization of the equivalent homogenized continuum to capture the behavior of the solid. $\Omega_f^{(b)}$ is the remaining part of the computational domain. In order to limit the MD region, a set of impedance forces needs to be applied along the boundaries of $\Omega_f^{(a)}$ to account for the interactions with the neighboring portion of the domain, as shown in Figure 1. The technique to eliminate the unwanted degrees of freedom, detailed in [14, 26, 51], exploited the periodic nature of the crystal structure in the MD region and made use of Green's function approach for the derivation of non-reflecting boundary conditions described by Karpov *et al.* [12]. Based on this coarse-fine decomposition, Tang *et al.* [56, 57] have derived higher-order approximations of the BSM. In addition, a phonon heat bath has been theoretically established that does not require empirical constants [57–59].

After the condensation procedure, the fine scale equations of motion assume the form:

$$\mathbf{M}_A \ddot{\mathbf{q}}(t) = \mathbf{f}(t) + \mathbf{f}^{\text{imp}}(t) + \mathbf{R}(t) \quad (15)$$

where $\mathbf{f}^{\text{imp}}(t)$ is an array of impedance forces, resembling the generalized Langevin equation proposed by Adelman and Doll [46, 47] and used in the method by Cai *et al.* [48] and $\mathbf{R}(t)$ is a random function that accounts for thermal atomic motion in the coarse scale (this quantity can be

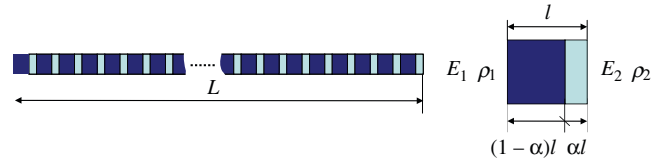


Figure 2. Schematic of bi-material rod and relative representative volume element (RVE).

neglected for multiscale continuum–continuum coupling in structural applications [26, 55]). The quantity $\mathbf{f}^{\text{imp}}(t)$ can be expressed as:

$$\mathbf{f}^{\text{imp}}(t) = \int_0^t \Theta(t - \tau)(\mathbf{q}(\tau) - \bar{\mathbf{u}}(\tau) - \mathbf{R}(\tau)) d\tau \quad (16)$$

The quantity Θ in Equation (16) is called *time-history kernel function* (or memory kernel function [60]) and describes the renormalization of the atomic interaction along the boundary of the reduced MD domain. As pointed out in [26, 51, 60], one of the challenges in the evaluation of Equation (16) consists of evaluating an inverse Laplace transform, which, in most cases, can only be carried out numerically. Among the existing methods for the calculation of inverse Laplace transforms, most authors working on BSM have used variations of the Weeks method [61] based on expansions in terms of Laguerre polynomials. In order to avoid the complexity of the Weeks scheme, Farrell *et al.* [62] have proposed to use the Crump method [63], based on a Fourier series approximation, and have shown that it requires fewer expansion terms than the Weeks method for comparable overall accuracy.

3.3. Applications

As a result of the non-reflective boundary conditions implemented at the interfaces, the BSM is particularly powerful for studying wave propagation problems. The extent of this capability has been investigated by Kadowaki and Liu [26] and Gonella and Ruzzene [55]. In the latter paper, the authors have investigated the propagation of axial waves in a bi-material rod with localized defects. The structure, depicted in Figure 2, consists of a periodic sequence of unit cells with alternating material properties. A first-order approximation of the dynamic behavior of the rod can be obtained by considering equivalent homogenized properties defined according to the classical rule of mixtures:

$$\rho_H = \rho_1 \alpha + \rho_2 (1 - \alpha) \quad (17)$$

$$E_H = \frac{E_1 E_2}{E_1 (1 - \alpha) + E_2 \alpha} \quad (18)$$

A defect is introduced in the model in the form of a soft inclusion by reducing Young’s modulus of one of the material layers. In order to capture the interaction of the propagating wave with the defect, a fine scale mesh is adopted in a small window corresponding to the neighborhood of the discontinuity. In this region, the material layers are modeled explicitly. Alongside the fine scale solution, a coarse scale solution is sought on an equivalent rod, with properties ρ_H and E_H , which is discretized with a low number of elements (Figure 3).

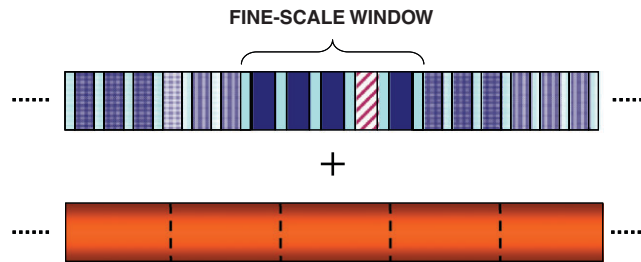


Figure 3. Fine scale window and homogenized model for a biomaterial rod.

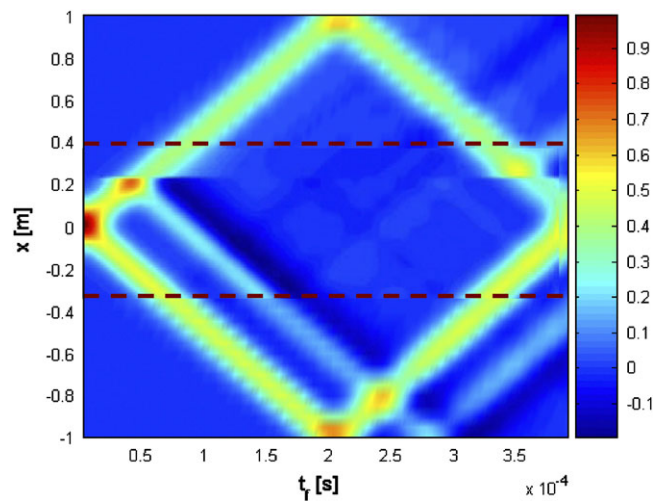


Figure 4. Wave propagation in a bi-material rod with soft inclusion. Fine scale solution superimposed to coarse scale solution.

An initial Gaussian distribution of displacements is applied to the midpoint of the structure. The resulting wave field is plotted against time and space in Figure 4 for the time necessary for the traveling wave to reach the free ends of the rod and travel back.

Figure 4 shows the fine scale solution, which is explicitly calculated in the central region of the domain, superimposed to the coarse scale solution, which is available everywhere. The purpose of the plot is to highlight the seamless transition between the scales and show how the spurious numerical reflections, due to the mismatch in mesh size, arising at the interface between the scales (marked by the dashed lines) are minimized. The coarse scale simulation provides a global description of the wave motion in the rod, but is insufficient to capture the details of the wave field generated by the interaction of the wave with the defect, as the element size in the coarse mesh is much larger than the size of the inclusion. On the contrary, the fine scale simulation provides an accurate local representation of the scattering phenomena triggered by the inclusion. A similar pattern is captured with comparable accuracy when the returning wave travels across the damage region. The lack of spurious reflections at the interfaces allows a straightforward interpretation

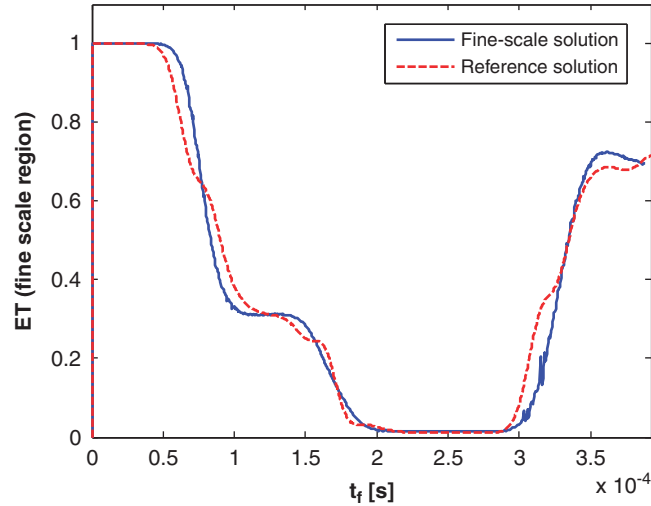


Figure 5. Total mechanical energy of fine scale region. BSM vs reference solution.

of the actual reflections due to the material discontinuity in the model. This property makes the method ideal for the simulation of waves in damaged structures for wave-based structural health monitoring applications. One way to quantify the accuracy of the technique consists of calculating the total mechanical energy inside the fine scale region and compares it against the same quantity evaluated through a fully detailed discretization over the whole domain. An example of comparison is shown in Figure 5. A discussion of the performance of the method for different combinations of materials and different wavelengths of excitation was given in [55].

Park *et al.* [15] have used the bridging scale method to investigate the problem of crack propagation in crystal structures. For this, they have considered a two-dimensional lattice domain and introduced initial anomalies in the crystal structure to cause initiation and growth of a crack under the effect of a traction load. In their work, an atomistic simulation was implemented in the neighborhood of the expected crack opening, while the superimposed coarse scale FE mesh extended to the two boundary regions, where homogenized material properties were prescribed. Since the traction loads were applied to the boundaries, where only the coarse scale solution was available, the disturbance introduced by the load had to travel first through the coarse scale and then across the interface before reaching the fine scale, where the crack began to propagate. Snapshots of three successive stages of crack propagation are shown in Figure 6. For sufficiently large velocities, the crack propagation resulted in complete fracture of the atomic lattice into two separate sections (Figure 6(c)). The authors of [15] have verified the accuracy of the method by comparing the multiscale simulation with a reference full MD solution obtained by setting an atomistic resolution throughout the computational domain. They have found virtually identical crack propagation speed and considerable agreement between the atomistic processes around the crack tips predicted by the two methods.

The BSM has also been successfully applied to study the problem of three-dimensional dynamic crack propagation in FCC crystals [14]. In this problem, the MD simulation was performed using a modified version of the Lennard–Jones 6–12 potential with a smooth cut-off. The computational

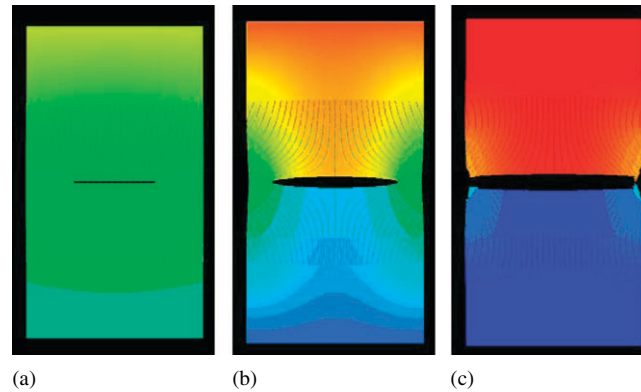


Figure 6. Bridging scale 2D modeling of crack propagation: (a) crack initiation phase; (b) crack growth phase; and (c) separation.

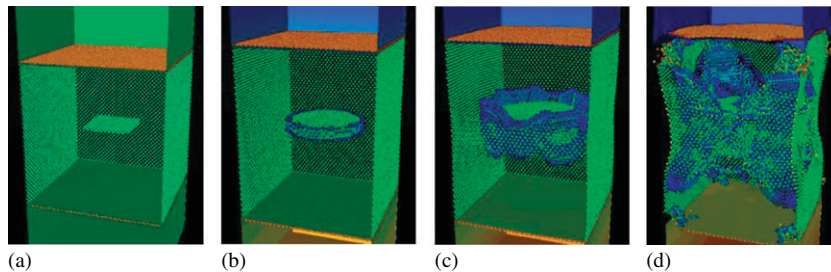


Figure 7. Successive stages of crack propagation: (a) initial crack; (b) crack growth; (c) onset of crack branching; and (d) out-of-plane crack branching.

domain was a parallelepiped, which was discretized with a coarse mesh of eight-node hexahedral elements. In the MD region located in the central part of the domain, a pre-crack was modeled by prescribing that two adjacent planes of atoms did not interact, such that the crack opened naturally following a mode-I type failure when a tensile load was applied to the boundaries. The bridging scale simulation required 1024 eight-node hexahedral elements and 117 121 atoms. In contrast, a reference solution was obtained through a fully detailed MD simulation involving 225 121 atoms. The time marching scheme used for the MD simulation had a time step $\Delta t_{\text{MD}} = 0.014$, whereas the time step of the coarse scale update was $\Delta t_{\text{FE}} = 20\Delta t_{\text{MD}}$. The MD region was bounded by six faces: two of them were shared with the pure FE region of the domain and were handled through non-reflective boundary conditions, whereas the other six were taken as free surfaces. The results of a simulation obtained using the Sandia-developed code Tahoe are shown in Figure 7.

3.4. Extension to space–time formulation

In many applications, the physics of interests are governed by multiple temporal scales as well as multiple spatial scales. Motivated by this, a space–time version of the BSM has been recently developed by Qian and Chirputkar [64]. The proposed approach has three key components: the extension

of the space–time FE method [65, 66] to discrete atomic systems, the multiscale approximation based on the extended finite element method (XFEM) [67–69] using space–time enrichment, and coupling with atomistic simulation methods through the BSM.

In the space–time FEM formulation, the approximations are expressed in terms of both space \mathbf{x} and time t . In a general three-dimensional case

$$\mathbf{u}(\mathbf{x}, t) = \sum_I \mathbf{N}_I(\mathbf{x}, t) \mathbf{d}_I \quad (19)$$

in which $\mathbf{N}_I(\mathbf{x}, t)$ is a set of FE shape functions at nodes indexed by I , and \mathbf{d}_I is the corresponding nodal displacement vector. Because of the ability to establish approximations in the temporal domain through the shape functions, the formulation can be extended to address the problems that involve multiple time scales. Qian and Chirputkar [64] have further applied the enrichment approach based on the XFEM [70, 71]. Assuming that $\phi(\mathbf{x}, t)$ is a certain function that represents the local physics, the approximation of the displacement based on the enrichment scheme is given as

$$\mathbf{u}^h(\mathbf{x}, t) = \bar{\mathbf{u}}^h(\mathbf{x}, t) + \tilde{\mathbf{u}}^h(\mathbf{x}, t) = \sum_{I \in \tilde{N}} \mathbf{N}_I(\mathbf{x}, t) \mathbf{d}_I + \sum_{J \in \tilde{N}} \mathbf{N}_J(\mathbf{x}, t) (\phi(\mathbf{x}, t) - \phi(\mathbf{x}_J, t_J)) \mathbf{a}_J \quad (20)$$

in which $\mathbf{N}_I(\mathbf{x}, t)$ are the regular space/time FE shape functions, \mathbf{x} is the material coordinate and $\phi(\mathbf{x}, t)$ is the enrichment function. Correspondingly, \mathbf{d}_I is the vector of nodal displacements, and \mathbf{a}_J is the vector of enriched degrees of freedom. The terms $\bar{\mathbf{u}}^h(\mathbf{x}, t)$ and $\tilde{\mathbf{u}}^h(\mathbf{x}, t)$ are the coarse and fine scale components of the space–time approximation that correspond to their counter parts on the RHS of Equation (20). This decomposition, which is the same as the one developed in the original BSM approach (Equation (8)), provides an additional vehicle for incorporating the important time scales that cannot be accommodated by the semi-discrete method.

The scheme for coupling the extended space–time FEM with molecular dynamics is illustrated in Figure 8. An overlapping scheme is used in the coupled region. The coupling is implemented in both the spatial and temporal domains. In the spatial domain, a combination of the projection operator based on the enriched approximation and the interfacial boundary condition treatment using the BSM described earlier is implemented. In the time domain, a multi-time-step algorithm is applied by taking advantage of the stability properties of the space–time formulation. For implementation details, we refer to [64].

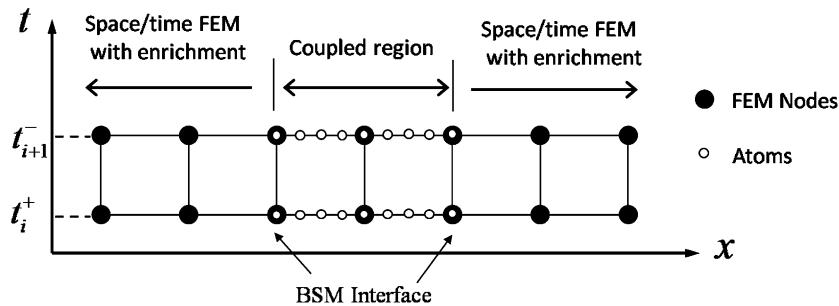


Figure 8. Coupling of extended space–time FEM with atomistic simulations.

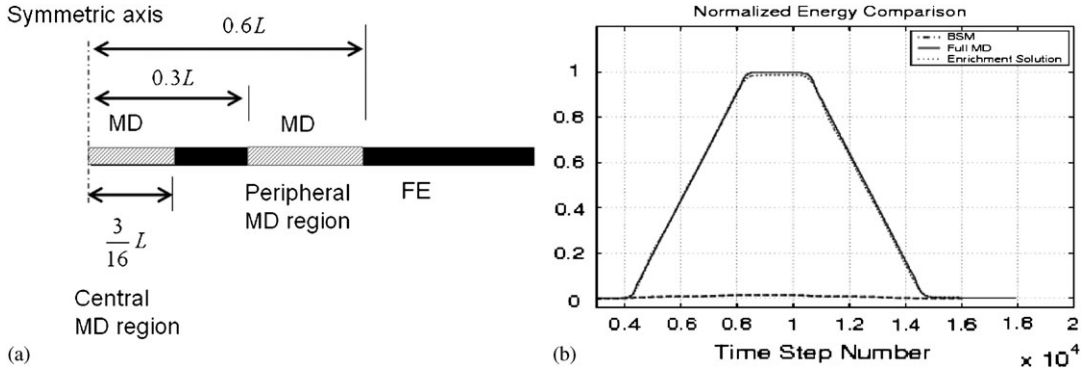


Figure 9. (a) Multiscale discretization for the 1D problem solved using space–time approach and (b) comparison of the energy history for the 2nd MD region.

The ability of this method in terms of achieving a reflectionless, wave-transmitting and energy conservative interfacial boundary condition is demonstrated in the following 1D problem shown in Figure 9(a). The entire domain is discretized using FEs. In addition, two MD regions are prescribed. A combination of coarse and fine scales is imposed in the first MD region next to the symmetric axis to examine how the wave propagates into the second MD region as a result of the developed scheme. For the purpose of verification, the results are compared with full-scale MD simulations and the standard bridging scale approach without the enrichment. This comparison is summarized in Figure 9(b). One can see that there are big differences between the results generated with and without enrichment. The amount of energy (plotted are normalized values) transmitted into the peripheral MD region is extremely low when no enrichment term is employed. By comparing these results with those from the full-scale MD simulation, it can be concluded that the wave transmitting boundary condition is successfully realized.

3.5. Multiscale non-equilibrium simulation method based on the bridging scale concept

Recently, Li and his co-workers have developed a multiscale non-equilibrium simulation method, or multiscale non-equilibrium molecular dynamics (MS-NEMD) [72–75], which can be used to simulate a host of non-equilibrium phenomena at small scales. The foundation of the concurrent multiscale non-equilibrium simulation is the bridging scale decomposition proposed in [51], which decomposes the discrete atomistic displacement field \mathbf{u} into a coarse scale part and a fine scale part as described by Equation (8). The main ingredients of the proposed MS-NEMD are its multiscale computation and coupling algorithms. A conceptual illustration of the multiscale framework is shown in Figure 10. In the proposed MS-NEMD model, it is argued that each coarse-scale FE node may be viewed as a thermal reservoir, and it represents the center of mass of an ensemble of atoms. Each set of atoms surrounding an FE node is called a Voronoi cell-ensemble. Since Voronoi cell or Voronoi tessellation is a dual structure of Delaunay triangulation [76], the cell structure is related to the FE mesh or discretization (Figure 10).

The classical canonical ensemble is a system embedded into an infinitely large thermal reservoir, whose temperature remains constant during an equilibrium process. In the MS-NEMD model, we argue that the temperature of each coarse scale nodal reservoir remains constant during any

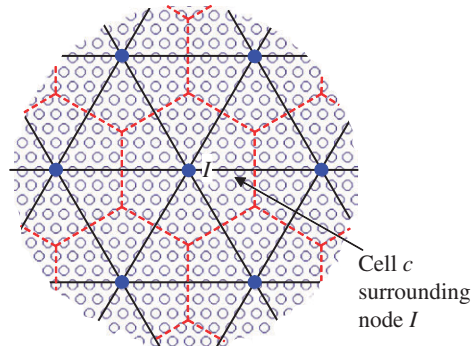


Figure 10. Coarse-grained finite element mesh and Voronoi cell-ensemble structure. (From Li and Sheng, 'On multiscale non-equilibrium molecular dynamics simulations', also in this issue.)

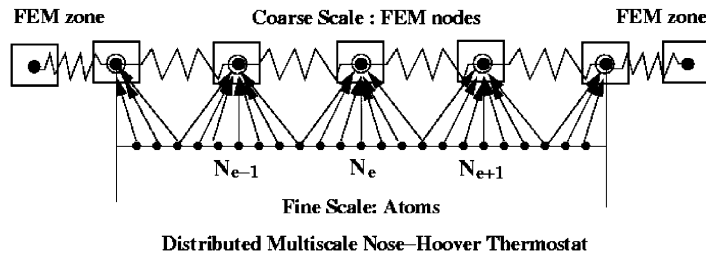


Figure 11. Structure of a distributed Nose-Hoover thermostat network.

time interval that is smaller than the time scale of the coarse grain system, which is chosen here as the coarse scale time step. Since a Voronoi cell-ensemble is embedded within a coarse scale nodal reservoir, the motions of atoms in a Voronoi cell-ensemble may reach a local equilibrium state within one coarse scale time step. We may then call a Voronoi cell-ensemble as a *multiscale canonical ensemble* in the sense of local equilibrium approximation. To ensure that each Voronoi cell-ensemble reaches a local equilibrium state in a coarse scale time step, we introduce a local Nose-Hoover thermostat in each cell-ensemble. The local thermodynamic temperature for each cell-ensemble is set as the coarse scale temperature at the governing FE node. Since the coarse scale temperature distribution is non-uniform and evolving with time, the FE nodal temperature changes from node to node and from time to time. Therefore, the local thermodynamic temperature is not uniform among different cell-ensembles and different coarse scale time steps. This requires the use of a *distributed Nose-Hoover thermostat network* (Figure 11) to regulate the local equilibrium state.

In statistical physics, the fluctuation dissipation theorem states that the response of a system in thermodynamic equilibrium to a small external perturbation is equivalent to its response to a spontaneous fluctuation. In the MS-NEMD model, the coarse scale thermodynamic temperature provides the external disturbance through the distributed Nose-Hoover thermostat network, which drives the system out of equilibrium, and it is equivalent to fluctuations created by random forces.

3.5.1. *Fine scale NEMD Model.* The multiscale displacement decomposition in Equation (8) implies similar decompositions for the velocity field $\dot{\mathbf{u}}$, and the linear momentum field \mathbf{p} , i.e.

$$\dot{\mathbf{u}} = \dot{\bar{\mathbf{u}}} + \dot{\tilde{\mathbf{u}}} \quad \text{and} \quad \mathbf{p} = \bar{\mathbf{p}} + \tilde{\mathbf{p}} \quad (21)$$

According to the bridging scale formulation [51], the total scale kinetic energy can be decoupled in terms of $\bar{\mathbf{p}}$ and $\tilde{\mathbf{p}}$. This leads to the following multiscale adiabatic Hamiltonian for a single cell-ensemble c surrounding the FE node I

$$H_c^{\text{adia}} = \sum_{i=1}^{n_{ce}} \frac{1}{2m_i} \bar{\mathbf{p}}_i \cdot \bar{\mathbf{p}}_i + \sum_{i=1}^{n_{ce}} \frac{1}{2m_i} \tilde{\mathbf{p}}_i \cdot \tilde{\mathbf{p}}_i + U(\mathbf{u}) \quad (22)$$

where n_{ce} is the number of atoms in the cell-ensemble c , $U(\mathbf{u})$ is the atomistic potential, $\bar{\mathbf{p}}_i$ and $\tilde{\mathbf{p}}_i$ are the coarse scale and fine scale linear momentum vectors of the i th atom, respectively. Here and in the following the subscript i is used to denote the quantities associated with the i th atom. Note that each cell-ensemble has only one node, hence, the numberings I and c have one-to-one correspondence (Figure 11). The two-scale equations of motion are then derived from Equation (22) as

$$\dot{\mathbf{u}}_i = \frac{\partial H_c^{\text{adia}}}{\partial \bar{\mathbf{p}}_i} = \frac{\bar{\mathbf{p}}_i}{m_i} + \frac{\tilde{\mathbf{p}}_i}{m_i} \quad \text{and} \quad \dot{\mathbf{p}}_i = -\frac{\partial H_c^{\text{adia}}}{\partial \mathbf{u}_i} = -\frac{\partial U(\mathbf{u})}{\partial \mathbf{u}_i} = \mathbf{F}_i \quad (23)$$

$$\dot{\mathbf{u}}_i = \frac{\partial H_c^{\text{adia}}}{\partial \tilde{\mathbf{p}}_i} = \frac{\tilde{\mathbf{p}}_i}{m_i} \quad \text{and} \quad \dot{\mathbf{p}}_i = -\frac{\partial H_c^{\text{adia}}}{\partial \tilde{\mathbf{q}}_i} = \mathbf{F}_j \cdot \frac{\partial \mathbf{q}_j}{\partial \tilde{\mathbf{u}}_i} \quad (24)$$

where \mathbf{F}_i denotes the external force acting on the atom i . From Equation (23), the fine scale equations of motion may be expressed in terms of \mathbf{u}_i and $\tilde{\mathbf{p}}_i$ as follows:

$$\dot{\mathbf{u}}_i = \frac{\bar{\mathbf{p}}_i}{m_i} + \frac{\tilde{\mathbf{p}}_i}{m_i} \quad \text{and} \quad \dot{\tilde{\mathbf{p}}}_i = \mathbf{F}_i - \dot{\bar{\mathbf{p}}}_i. \quad (25)$$

To couple the fine scale motions of atoms with the coarse scale heat conduction, we introduce a local Nose–Hoover thermostat in each cell-ensemble such that the fine scale equations of motion (Equation (25)) become

$$\dot{\mathbf{u}}_i = \frac{\bar{\mathbf{p}}_i}{m_i} + \frac{\tilde{\mathbf{p}}_i}{m_i} \quad \text{and} \quad \dot{\tilde{\mathbf{p}}}_i = \mathbf{F}_i - \dot{\bar{\mathbf{p}}}_i - \zeta_c \tilde{\mathbf{p}}_i \quad (26)$$

$$\forall i \in \mathbf{n}_c, \quad \mathbf{n}_c = \{1, \dots, n_{ce}\} \quad \text{and} \quad \dot{\zeta}_c = \frac{1}{\Theta_c} \left(\sum_{i \in \mathbf{n}_c} \frac{\tilde{\mathbf{p}}_i \cdot \tilde{\mathbf{p}}_i}{m_i} - 3n_c k_B T_c \right) \quad (27)$$

where k_B is the Boltzmann constant, ζ_c is an auxiliary variable [77–79], Θ_c is the pseudo mass of ζ_c , and the local thermodynamic temperature T_c for cell-ensemble c is the coarse scale temperature at the governing FE node I .

3.5.2. *Coarse scale model.* In the discrete-to-continuum multiscale computations, we want our coarse scale model to be consistent with the fine scale model. This means that we have to incorporate atomic information into the coarse scale level. Traditional FE methods do not satisfy this criterion, since they use empirical constitutive models. In the proposed MS-NEMD model, the coarse scale

mean field is concurrently solved by the FE method based on a coarse-grained thermodynamics model. The formulation is based on a coarse-grained Helmholtz free energy. It stems from the principles described in [80] and is derived with the assumptions of harmonic approximation and the Cauchy–Born rule. In this paper, we will use the coarse-grained Helmholtz free energy to derive macroscopic quantities in coupled thermomechanical equations.

Based on the harmonic approximation and the Cauchy–Born rule, the coarse-grained Helmholtz free energy in a cell-ensemble c may be written as [80]

$$\Phi^c(\bar{\mathbf{F}}^c, T_c) = U(\bar{\mathbf{F}}^c) + k_B T_c \sum_{i=1}^{n_{ce}} \sum_{k=1}^3 \log \left[2 \sinh \left(\frac{\hbar \omega_{ik}(\bar{\mathbf{F}}^c)}{4\pi k_B T_c} \right) \right] \quad (28)$$

where \hbar is Planck’s constant divided by 2π ; T_c is the coarse scale thermodynamic temperature for the cell-ensemble c ; and ω_{ik} are three normal mode frequencies for the atom i , which depend on $\bar{\mathbf{F}}^c$ through $\bar{\mathbf{r}}_{i\alpha}$ and can be determined via harmonic approximation [81]. Note that in the proposed MS-NEMD model, T_c is updated based on fine scale atomistic velocities:

$$T_c = \frac{2}{3(n_c - 1)k_B} \left\langle \sum_{i=1}^{n_{ce}} \frac{\tilde{\mathbf{p}}_i \cdot \tilde{\mathbf{p}}_i}{2m_i} \right\rangle \quad (29)$$

where $\langle \cdot \rangle$ denotes averaging in time. With Φ^c available, we can derive the expressions for the state variables such as the first Piola–Kirchhoff stress \mathbf{P}^c ,

$$\begin{aligned} \mathbf{P}^c(\bar{\mathbf{F}}^c, T_c) &= \frac{1}{\Omega_c} \frac{\partial \Phi^c}{\partial \bar{\mathbf{F}}^c} = \frac{1}{\Omega_c} \left\{ \frac{1}{2} \sum_{i=1}^{n_{ce}} \sum_{\alpha=1}^{n_b} \phi'(\bar{r}_{i\alpha}) \frac{\bar{\mathbf{r}}_{i\alpha} \otimes \mathbf{R}_{i\alpha}}{\bar{r}_{i\alpha}} \right. \\ &\quad \left. + \frac{\hbar}{4\pi} \sum_{i=1}^{n_{ce}} \sum_{k=1}^3 \coth \left(\frac{\hbar \omega_{ik}(\bar{\mathbf{F}}^c)}{4\pi k_B T_c} \right) \left[\sum_{\alpha=1}^{n_b} \omega'_{ik}(\bar{r}_{i\alpha}) \frac{\bar{\mathbf{r}}_{i\alpha} \otimes \mathbf{R}_{i\alpha}}{\bar{r}_{i\alpha}} \right] \right\} \quad (30) \end{aligned}$$

in which Ω_c denotes the volume of the cell-ensemble c . Note that in the proposed MS-NEMD algorithm, the above transport coefficients will be later updated based on the fine scale computation via the response theory.

We have also performed the direct NEMD simulation with a prescribed temperature of 200 K at boundary. The results are compared with that of the MS-NEMD simulation with the initial temperature of 200 K. It is found that the direct NEMD simulation fails to predict thermal-activation of shock wave or dislocation, whereas the MS-NEMD simulation can do so, Figure 12(a) and (b). By comparing the instantaneous temperature profiles obtained by the two simulations in Figure 12(c) and (d), it is observed that the instantaneous temperature distribution obtained by the MS-NEMD simulation exhibits larger fluctuations than that of the direct NEMD simulation.

4. MULTIREOLUTION CONTINUUM THEORY

A general multiscale theory for heterogeneous materials, called multiresolution continuum theory (MRCT), has been proposed by Liu and coworkers [35–38, 82]. This theory inherits the idea from the BSM, but uses a single discretization with the additional scales approximated by additional degrees of freedom. It is proposed to overcome the limitations of a conventional continuum approach, existing higher-order/gradient models and direct coupling schemes. This approach is

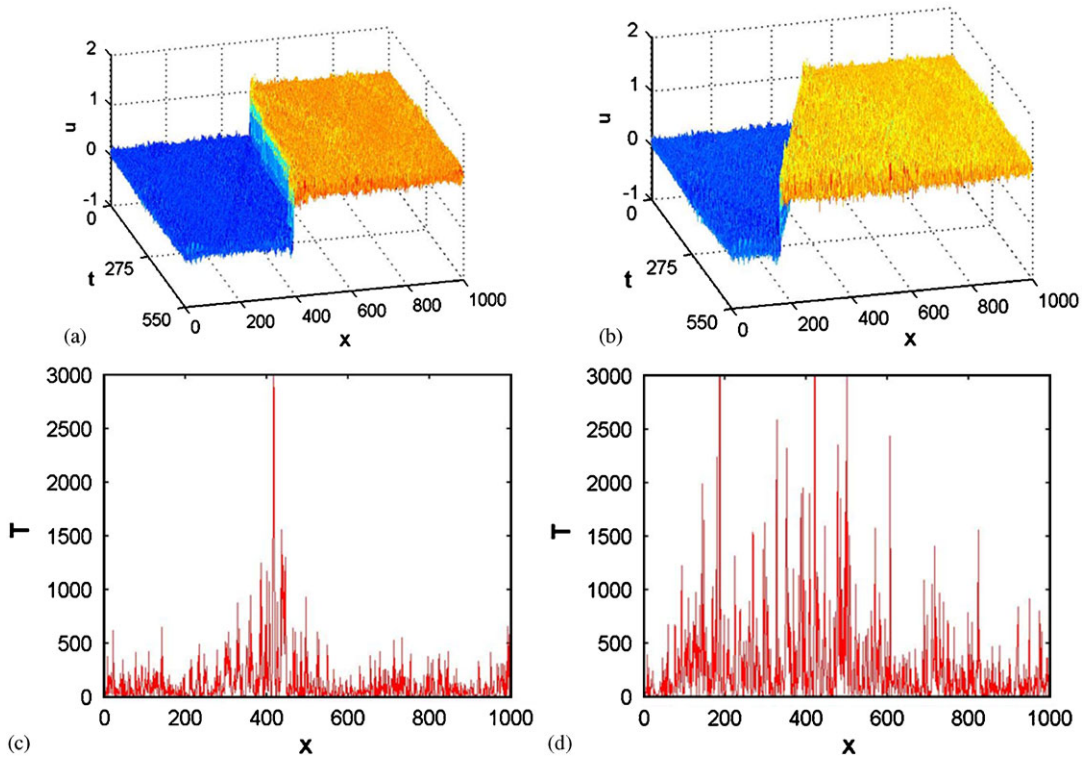


Figure 12. Displacement profiles obtained by (a) direct NEMD simulation and (b) MS-NEMD simulation; instantaneous temperature profiles obtained by (c) direct NEMD simulation and (d) MS-NEMD simulation.

characterized by some key features:

- It allows macroscale properties (e.g. strength, hardness, and toughness) and global structure performance to be predicted directly in terms of key microstructure parameters, such as the length scales of inhomogeneous deformation.
- By providing a clear mathematical link between materials microstructure and structural properties, it can be used to monitor structural health accounting for manufacturing tolerances and mission-specified operation conditions.

The method is based on a virtual power decomposition performed on multiple nested domains and applies to materials that feature a highly inhomogeneous deformation at or below the scale of their RVE, deformation which often results in terminal strain localization.

4.1. General theory

The conventional homogenization approach requires that the continuum virtual power density field δp at a material point (\mathbf{x}) in the homogenized domain can be expressed as

$$\delta p^{\text{hom}}(\mathbf{x}) = \frac{1}{V_0} \int_{V_0} \delta p_m dV_0 = \frac{1}{V_0} \int_{V_0} \boldsymbol{\sigma}_m : \delta \mathbf{L}_m dV_0 = \boldsymbol{\sigma}(\mathbf{x}) : \delta \mathbf{L}(\mathbf{x}) \quad (31)$$

where V_0 is the volume of the RVE centered at the continuum point \mathbf{x} , $\boldsymbol{\sigma}_m$ and \mathbf{L}_m are local stress and velocity gradient fields, $\boldsymbol{\sigma}$ and \mathbf{L} are the average stress and velocity gradient within the RVE, and the last equality follows from the Hill–Mandel lemma [83]. In the multiresolution theory, the Hill–Mandel approach is extended to account for both homogeneous and inhomogeneous contributions, so that:

$$\delta p(\mathbf{x}) = \delta p^{\text{hom}}(\mathbf{x}) + \delta p^{\text{inh}}(\mathbf{x}) \quad (32)$$

where the inhomogeneous term is defined as the difference between the average virtual power density at the inhomogeneous deformation scale V_1 and the average virtual power density at the RVE scale:

$$\delta p^{\text{inh}}(\mathbf{x}) = \frac{1}{V_1} \int_{V_1} (\boldsymbol{\sigma}_m : \delta \mathbf{L}_m) dV_1 - \boldsymbol{\sigma}(\mathbf{x}) : \delta \mathbf{L}(\mathbf{x}) = \frac{1}{V_1} \int_{V_1} (\boldsymbol{\sigma}_m : \delta \mathbf{L}_m - \boldsymbol{\sigma}(\mathbf{x}) : \delta \mathbf{L}(\mathbf{x})) dV_1 \quad (33)$$

The inhomogeneous power density δp^{inh} can be rewritten in terms of the local inhomogeneous velocity gradient $\mathbf{L}_m - \mathbf{L}$ as

$$\delta p^{\text{inh}}(\mathbf{x}) = \frac{1}{V_1} \int_{V_1} \boldsymbol{\beta}_m : (\delta \mathbf{L}_m - \delta \mathbf{L}(\mathbf{x})) dV_1 \quad (34)$$

where the local microstress $\boldsymbol{\beta}_m$ is introduced as the power conjugate of the local velocity gradient $\mathbf{L}_m - \mathbf{L}$, in order to enforce the following power equivalence:

$$\boldsymbol{\beta}_m : (\mathbf{L}_m - \mathbf{L}(\mathbf{x})) = \boldsymbol{\sigma}_m : \mathbf{L}_m - \boldsymbol{\sigma}(\mathbf{x}) : \mathbf{L}(\mathbf{x}) \quad (35)$$

It is furthermore assumed that the local velocity gradient \mathbf{L}_m varies linearly inside V_1 as

$$\mathbf{L}_m \approx \frac{1}{V_1} \int_{V_1} \mathbf{L}_m dV + \left(\frac{1}{V_1} \int_{V_1} \mathbf{L}_m \overset{\sim}{\nabla} dV \right) \cdot \mathbf{y} = \mathbf{L}^1(\mathbf{x}) + \mathbf{G}^1(\mathbf{x}) \cdot \mathbf{y} \quad (36)$$

where \mathbf{y} is the local position with respect to the center of V_1 and \mathbf{L}^1 and \mathbf{G}^1 are higher-order continuum measures corresponding to volume averages of the local velocity gradient \mathbf{L}_m and the spatial gradient of the local velocity gradient $\mathbf{L}_m \overset{\sim}{\nabla}$, respectively. Upon substitution of Equation (36) into Equation (35), the inhomogeneous virtual power term is rewritten as

$$\delta p^{\text{inh}}(\mathbf{x}) = \boldsymbol{\beta}^1(\mathbf{x}) : (\delta \mathbf{L}^1(\mathbf{x}) - \delta \mathbf{L}(\mathbf{x})) + \bar{\boldsymbol{\beta}}^1(\mathbf{x}) : \delta \mathbf{G}^1(\mathbf{x}) \quad (37)$$

where $\boldsymbol{\beta}^1$ is a continuum microstress and $\bar{\boldsymbol{\beta}}^1$ is a continuum microstress couple, respectively, defined as:

$$\boldsymbol{\beta}^1(\mathbf{x}) = \frac{1}{V_1} \int_{V_1} \boldsymbol{\beta}_m dV_1 \quad (38)$$

$$\bar{\boldsymbol{\beta}}^1(\mathbf{x}) = \frac{1}{V_1} \int_{V_1} \boldsymbol{\beta}_m \otimes \mathbf{y} dV_1 \quad (39)$$

In conclusion, the total virtual internal power density is written as:

$$\delta p = \boldsymbol{\sigma} : \delta \mathbf{L} + \boldsymbol{\beta}^1 : (\delta \mathbf{L}^1 - \delta \mathbf{L}) + \bar{\boldsymbol{\beta}}^1 : \delta \mathbf{G}^1 \quad (40)$$

The key feature of this approach is that the characteristic length-scale information is automatically embedded in the formulation through the averaging operations in Equations (38) and (39). An extension of this formulation has been proposed by Vernerey *et al.* [35] to account for the existence of multiple nested scales of inhomogeneous deformation. This formulation introduces a microstress and a microstress couple at each scale of deformation, such that the internal power density is a summation over all the inhomogeneous contributions:

$$\delta p^{\text{int}} = \boldsymbol{\sigma} : \delta \mathbf{L} + \sum_{n=1}^N (\boldsymbol{\beta}^n : (\delta \mathbf{L}^n - \delta \mathbf{L}) + \bar{\boldsymbol{\beta}}^n : \delta \mathbf{G}^n) \quad (41)$$

where the following generalizations of Equations (38) and (39) are used:

$$\boldsymbol{\beta}^n = \frac{1}{V_n} \int_{V_n} \boldsymbol{\beta}_m \, dV \quad (42)$$

$$\bar{\boldsymbol{\beta}}^n = \frac{1}{V_n} \int_{V_n} \boldsymbol{\beta}_m \otimes \mathbf{y} \, dV \quad (43)$$

4.2. Multiresolution governing equations

The virtual internal power is obtained by integrating the power density over the entire domain

$$\delta p^{\text{int}} = \int_V \left\{ \boldsymbol{\sigma} : \delta \mathbf{L} + \sum_{n=1}^N (\boldsymbol{\beta}^n : (\delta \mathbf{L}^n - \delta \mathbf{L}) + \bar{\boldsymbol{\beta}}^n : \delta \mathbf{G}^n) \right\} dV \quad (44)$$

The virtual kinetic power is based on the following extension of the expression presented in [27] to multiple scales [35]:

$$\delta p^{\text{kin}} = \int_V \left\{ \rho \dot{\mathbf{v}} \cdot \delta \mathbf{v} + \sum_{n=1}^N (\boldsymbol{\gamma}^n \cdot \mathbf{I}^n) : \delta \mathbf{L}^n \right\} dV \quad (45)$$

The expression in Equation (45) introduces an n th-scale microacceleration $\boldsymbol{\gamma}^n$ and a second moment of density \mathbf{I}^n , respectively, defined as

$$\boldsymbol{\gamma}^n = \dot{\mathbf{L}}^n + \mathbf{L}^n \cdot \mathbf{L}^n \quad (46)$$

$$\mathbf{I}^n = \frac{1}{V_n} \int_{V_n} \rho^n \mathbf{y}^n \otimes \mathbf{y}^n \, dV \quad (47)$$

where $\bar{\rho}^n$ and $\rho^n = \bar{\rho}^n - \bar{\rho}^{n-1}$ are the microscopic density and the relative density of the n th scale, respectively. Lastly, the multiscale external virtual power is obtained by extending the conventional external power expression:

$$\delta p^{\text{ext}} = \int_V \left\{ \mathbf{b} \cdot \delta \mathbf{v} + \sum_{n=1}^N \mathbf{B}^n : \delta \mathbf{L}^n \right\} dV + \int_{\Gamma_t} \left\{ \mathbf{t} \cdot \delta \mathbf{v} + \sum_{n=1}^N \mathbf{R}^n : \delta \mathbf{L}^n \right\} d\Gamma \quad (48)$$

where \mathbf{b} and \mathbf{t} are the conventional continuum body force and traction, whereas \mathbf{B}^n and \mathbf{R}^n are the corresponding multiscale terms. Similar to a conventional continuum, where applying a body force \mathbf{b} or a surface traction \mathbf{t} drives a velocity gradient \mathbf{L} in the solid, in this formulation the

body couple stress \mathbf{B}^n and double traction force \mathbf{R}^n will establish the inhomogeneous velocity gradient $\mathbf{L}^n - \mathbf{L}$ in the domain. By application of the divergence theorem, and making use of the arbitrariness of the variations $\delta \mathbf{v}$ and $\delta \mathbf{L}^n$, it is possible to derive a strong form of the multiscale equations of motion [37]:

$$\begin{aligned} \left(\boldsymbol{\sigma} - \sum_{n=1}^N \boldsymbol{\beta}^n \right) \cdot \nabla + \mathbf{b} &= \rho \dot{\mathbf{v}} \quad \text{in } V \\ \bar{\boldsymbol{\beta}}^n \cdot \nabla - \boldsymbol{\beta}^n + \mathbf{B}^n &= \boldsymbol{\gamma} \cdot \mathbf{I}^n \quad \text{in } V \end{aligned} \quad (49)$$

with relative multiscale boundary conditions

$$\begin{aligned} \mathbf{n} \cdot \left(\boldsymbol{\sigma} - \sum_{n=1}^N \boldsymbol{\beta}^n \right) &= \mathbf{t} \quad \text{on } \Gamma_t \\ \mathbf{n} \cdot \bar{\boldsymbol{\beta}}^n &= \mathbf{R}^n \quad \text{on } \Gamma_{R^n} \end{aligned} \quad (50)$$

where Γ_t and Γ_{R^n} are the boundaries of the RVE and of the n th volume, respectively. These multiscale equations can be solved numerically through an FE technique involving generalized multiscale nodal degrees of freedom [35].

4.3. Multiresolution constitutive relations

In order to solve the multiresolution continuum equations, the following constitutive relations are required:

$$\dot{\boldsymbol{\sigma}} = \dot{\boldsymbol{\sigma}}(\mathbf{L}) \quad \dot{\boldsymbol{\beta}}^n = \dot{\boldsymbol{\beta}}^n(\mathbf{L}^n - \mathbf{L}) \quad \dot{\bar{\boldsymbol{\beta}}}^n = \dot{\bar{\boldsymbol{\beta}}}^n(\mathbf{G}^n) \quad (51)$$

When dealing with the microscale constitutive relationship, the inhomogeneous rate of deformation $\mathbf{D}^n - \mathbf{D}$ is considered (i.e. the symmetric part of the inhomogeneous velocity gradient $\mathbf{L}^n - \mathbf{L}$). Developing higher-order constitutive relationships such as $\dot{\bar{\boldsymbol{\beta}}}^n(\mathbf{G}^n)$ has been one of the key challenges of second gradient methods.

While macroscopic constitutive models for elasticity and plasticity are fairly straightforward, many of the efforts in [36–38, 84] have been directed towards the tougher goal of developing the higher-order constitutive models $\dot{\boldsymbol{\beta}}^n(\mathbf{L}^n - \mathbf{L})$ and $\dot{\bar{\boldsymbol{\beta}}}^n(\mathbf{G}^n)$. The details of this part of the formulation are summarized effectively in [37] and will not be reported here. Nevertheless, it is worth pointing out a few unique aspects of the method with respect to the derivation of the microscopic constitutive equations. Each of the constitutive models in Equation (51) can be calibrated from refined computational models of the microstructure through averaging operations performed at each scale V_n within the selected RVE. The main steps of the stress/strain calculation and calibration procedure at each microscopic scale are listed below:

- A conventional RVE (macroscopic volume) is defined and loaded under several boundary conditions.
- Average stress and strain measures are recorded and used to calibrate the macroscale constitutive models.
- Regions of highly inhomogeneous deformation are identified in the RVE. An appropriate averaging volume is selected at the scale of this microscopic deformation.

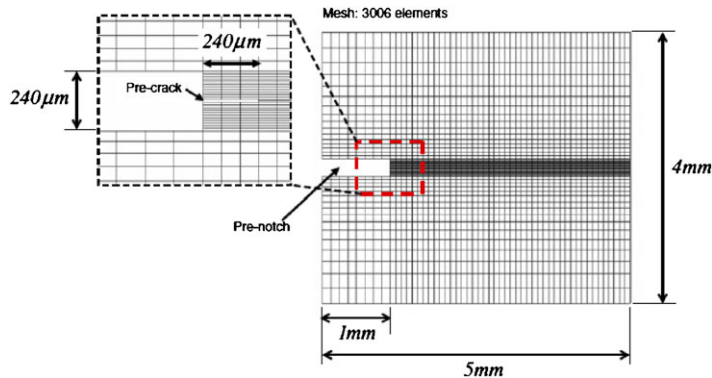


Figure 13. Setup for shear band problem. (Reprinted from [37], copyright 2008, with permission from Elsevier.)

- A relative strain measure is calculated as the difference between the average strain inside the local volume and the one inside RVE.
- The corresponding local average stress is obtained through a power equivalence and averaged over the volume.
- The relationship between relative strain and microstress is calibrated through an appropriate constitutive model.
- The average strain gradient and the corresponding average microstress moment are computed within the inhomogeneous averaging volume and calibrated.

4.4. Multiresolution analysis of adiabatic shear band

Over the past few years, the multiresolution theory has been applied to a number of topical problems in mechanics. McVeigh and Liu have used this method to study, among other problems, the formation and propagation of adiabatic shear band in steel alloys [37]. The multiscale nature of shear band phenomena makes them an excellent benchmark problem, as the deformation within the shear band is highly inhomogeneous and cannot be properly captured through a standard single-scale elasto-plastic model. The problem was set up as a two-dimensional plane-strain problem, as proposed by Medyanik *et al.* [85] and recalled in Figure 13. The plate was modeled with a macroscopic notch featuring a microscopic pre-crack at the notch tip.

In the neighborhood of the pre-crack, the mesh was chosen such that the elemental size was small enough to capture a shear band of the order of tens of microns, consistently with values commonly reported in the literature [86]. The macroscale constitutive law of the steel-alloy followed the Bammann–Chiesa–Johnston model, whose constants were calibrated to an empirical rate and temperature-dependent Johnson–Cook model [85]. The plastic part of the BCJ model also accounted for microvoid damage through microvoid damage equations developed using the computational cell modeling analysis of McVeigh *et al.* [87].

Since the macroscopic plastic stress–strain curve of the material showed a hardening region followed by instability and by a softening region, McVeigh *et al.* [37] have implemented a multiresolution scheme with two embedded length scales: the hardening length scale l^h , related to the grain size, and the softening scale l^v , dictated by the microvoid spacing. In order to test the validity

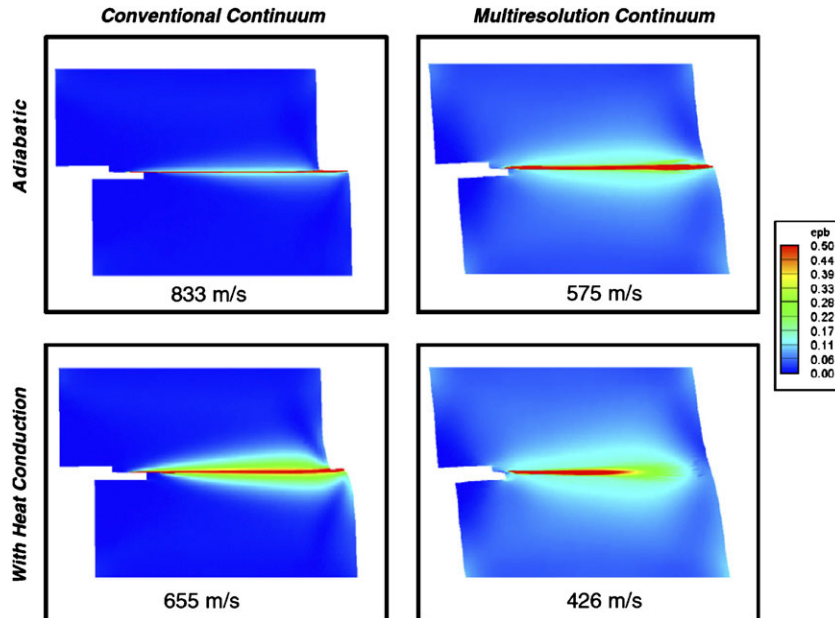


Figure 14. Conventional continuum and multiresolution simulations of shear band: Plastic strain. (Reprinted from [37], copyright 2008, with permission from Elsevier.)

of the method, the problem was solved both using conventional continuum as well as MRCTs. The simulation was performed both for adiabatic temperature rise and in the presence of heat conduction. The plastic strain contours are plotted in Figure 14.

The plastic strain across the shear band in the y -direction is plotted in Figure 15. It can be noted that, in the case of multiresolution, the deformation occurring during work hardening is relatively homogeneous. After nucleation is reached, the deformation localizes to the embedded scale l^v . McVeigh *et al.* pointed out that this is consistent with the physical interpretation of shear band, as reported, for instance, in [86]. The post-instability localization occurred at the length-scale l^v and spread over several elements. In contrast, it can be seen that conventional continuum localized the deformation in the central element of the domain in an unphysical manner. This contrast is particularly evident in the case of adiabatic shear band.

4.5. Multiresolution analysis of fracture in high-strength steel

The multiresolution theory has also been applied by Vernerey *et al.* [36], Siad *et al.*, [88] and McVeigh and Liu [89] in the analysis of ductile fracture processes. In Vernerey *et al.* [36], they considered high-strength steels with two populations of hard particles distributed at two distinct length scales in an alloy matrix. The distinct role of primary and secondary particles in ductile fracture phenomena can be deduced by observation of the fracture surface. Because bonding at the particle–matrix interface is stronger for secondary than for primary particles, nucleation, and growth of voids from primary particles occurs first. Once the voids reach a critical size, the local plastic strains lead to nucleation of microvoids at the sites of secondary particles, which eventually grow into a ‘void sheet’. Finally, failure occurs when the microvoids coalesce (Figure 16).

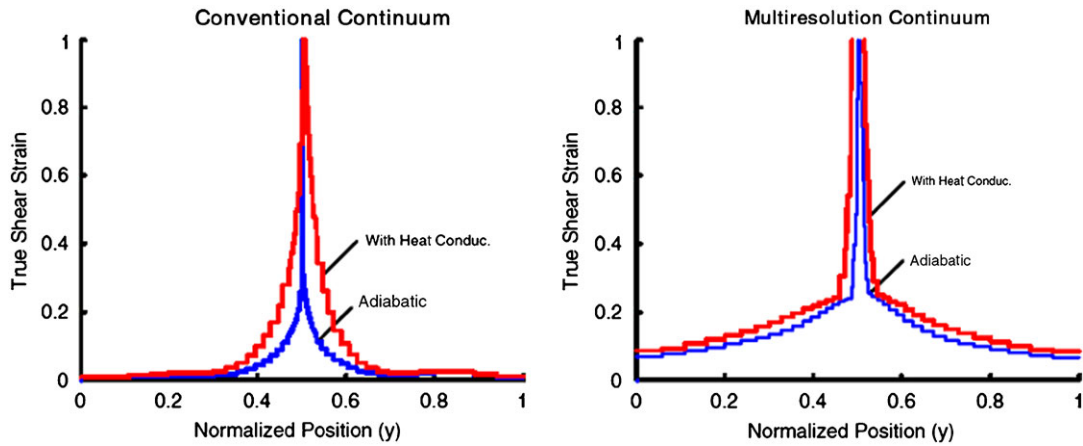


Figure 15. Conventional continuum and multiresolution simulations of shear band: values of plastic strain in the y -direction across the shear band. (Reprinted from [37], copyright 2008, with permission from Elsevier.)

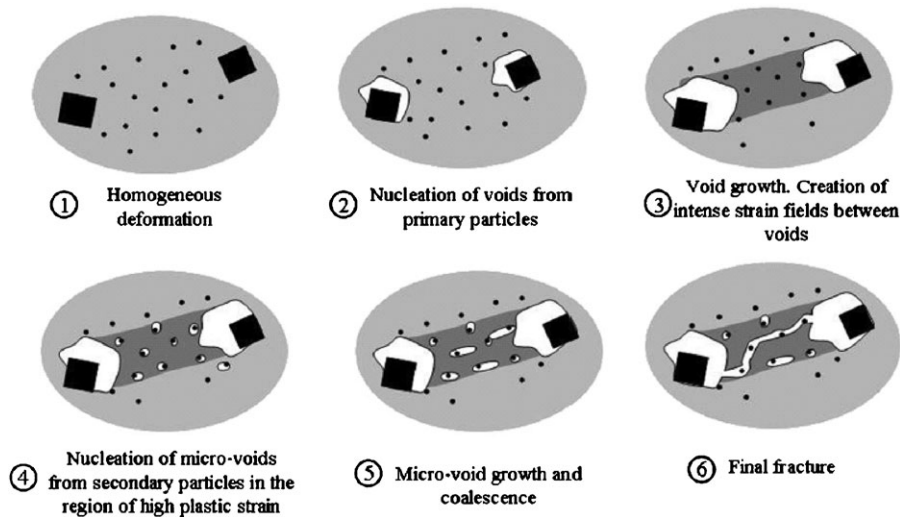


Figure 16. Stages of ductile fracture in high-strength steels. (Reprinted from [36], copyright 2008, with permission from Elsevier.)

In order to tackle this problem, a three-scale multiresolution formulation has been implemented. The macroscale is the scale of the specimen, the microscale is the scale determined by the primary particles and the sub-microscale is associated with the secondary particles. The three-scale model was applied to calculate the plastic strain field in a specimen in tension under plane-strain conditions, as shown in Figure 16. In order to trigger the localization, an imperfection was introduced at the center of the domain by reducing the yield stress of the central element by 5%. The symmetry of the

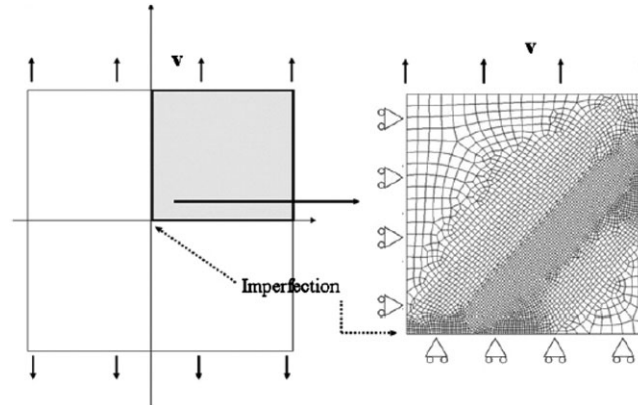


Figure 17. Geometry, boundary conditions and finite element discretization of the tensile specimen. (Reprinted from [36], copyright 2008, with permission from Elsevier.)

body was exploited to reduce the computational domain to a quarter cell. The FE mesh, consisting of 4121 quadrilateral elements having size comparable to the length scale of the secondary particles, is shown in Figure 17, together with the relative boundary conditions.

The evolution of the effective plastic strains at the macro, micro and sub-micro scales, shown in Figure 18, highlights the existence of three successive stages of material failure. The first stage corresponds to material instability due to the imperfection. The interaction between the damaged zone and the free surface results in a band of high plastic strain, with width dictated by the size of the primary particles, which in return determines the nucleation of voids from the primary particles. As the damage grows, the plastic strain in the shear band increases. Owing to the large shear strain levels near the free boundary, the criterion for the nucleation of secondary particles is first met in this region of the domain, resulting in a microstress instability that grows from the free boundary towards the center. This inner shear band due to microvoid growth has a width that is related to the size of the length scale of the sub-microscale. The final stage of the process is reached when the microvoids coalesce. In the multiscale model, microvoid coalescence can be observed to appear within the microshear band in the bottom right picture of Figure 18.

4.6. MRCT based on the Virtual Atom Cluster model

In the methods described earlier, the multiscale contributions to the virtual power are given in a continuum mechanics framework. However, the hierarchical or concurrent multiscale theories may also be used to examine a continuum and an atomic scale simultaneously through a coarse graining or atomic averaging theory. The Virtual Atomic Cluster (VAC) theory [63] works along these lines. Motivated by the discrepancies between the basic features of continuum and atomistic systems, the 'VAC' model has been developed by Qian *et al.* [21, 90]. The model is proposed as an effective representation of the interaction at the atomic scale and can be linked to coarse scale simulation methods such as meshfree or FEMs. The model is coarse grained and therefore ensures scalability at the numerical implementation level. However, as the model representation is discrete, continuum concepts such as strain and stress are completely removed. Furthermore,

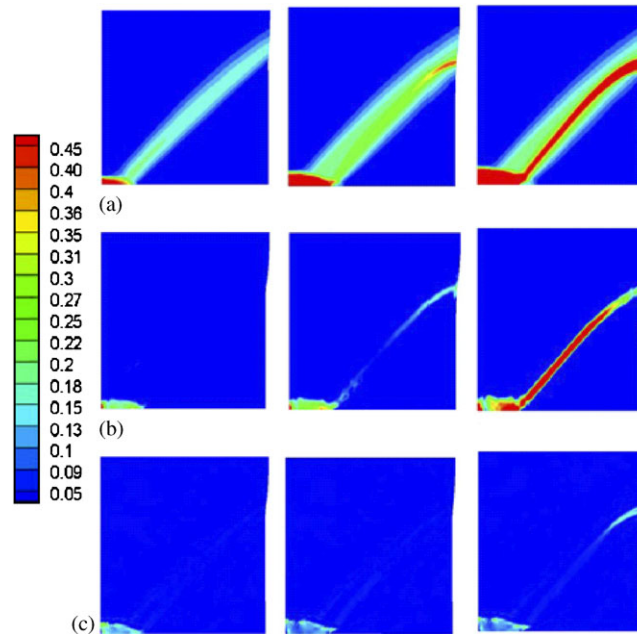


Figure 18. Evolution of plastic strain: (a) macroscale; (b) microscale; and (c) sub-microscale. (Reprinted from [36], copyright 2008, with permission from Elsevier.)

the model is also built based on the underlying inter-atomic mechanics, as in the crystal elasticity approach. This consistent link guarantees the accuracy in describing the mechanics of the nanostructure.

Figure 19 illustrates the steps required to construct the VAC for a graphene sheet. A VAC is the minimum set of atoms that forms a cluster fully representing the energy density, and can therefore be extracted from the lattice structure. The original molecular structure is then transformed into a structure of the same geometry with continuous energy density distribution. The energy density corresponding to any point within the geometry is represented by a VAC. The word ‘virtual’ comes from the fact that the VAC does not have to correspond to the physical atoms, and is thus regarded as a virtual representation.

Based on this model, one could replace the original molecular structure with a virtual structure of the same geometry but with distributed energy density. The energy density at any point within this structure is represented by a cluster of atoms, as shown in Figure 19. The cluster is chosen as a basic representation of the energy density, which ensures the equivalence of the energy between the molecular and virtual structures.

As shown in Figure 19, the discrete summation of the potential energy defined in the original molecular structure is now replaced with a continuous integral based on the use of the VAC model. In Figure 19, ϕ_i represents the potential energy of each atom and ϕ_ρ is the distributed energy density. The use of ϕ_ρ allows the use of arbitrary quadrature in the case of numerical implementation. The number of quadrature points can be far less than the actual number of atoms.

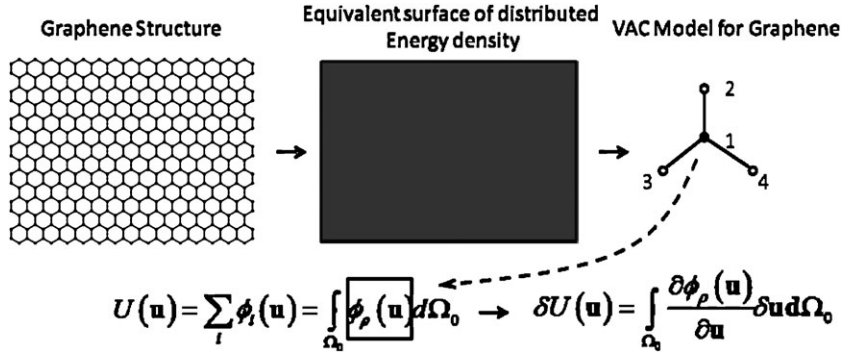


Figure 19. Steps to build the proposed VAC model for graphene sheet. The molecular model is converted to a structure of the same geometry with distributed energy density represented by VAC.

The variation of the internal energy density can then be evaluated by imposing the VAC model at each quadrature point. The VAC model in Figure 19 consists of four atoms, therefore

$$\delta\phi_\rho = \sum_{\alpha=1}^4 \frac{\partial U}{\partial \mathbf{u}_\alpha} \cdot \delta \mathbf{u}_\alpha = \sum_I \left(\sum_{\alpha=1}^4 \frac{\partial U}{\partial \mathbf{u}_\alpha} \mathbf{N}_{I\alpha} \right) \cdot \delta \mathbf{d}_I = \sum_I \mathbf{f}_{\rho I} \cdot \delta \mathbf{d}_I \quad (52)$$

in which \mathbf{u}_α is the displacement vector defined at atom α , and is interpolated by meshfree shape function $\mathbf{N}_{I\alpha}$, i.e. $\mathbf{u}_\alpha = \sum_I \mathbf{N}_{I\alpha} \mathbf{d}_I$ and \mathbf{d}_I is the displacement vector that is defined at the node. The contribution to the nodal internal force in the FEM/meshfree formulation now simply reads

$$\mathbf{F}_{IG}^{\text{int}} = w_G \mathbf{f}_{\rho I} \quad (53)$$

in which I is the index for the computational nodes and G the one for quadrature points, w is the weighting function corresponding to the quadrature points.

A multiscale VAC model can be developed by separating the material into two regions, Ω^0 and Ω^1 . The domain Ω^1 represents the region where homogenization theory is invalid, e.g. at a material interface or strain localization region. The scale zero internal power is computed as a homogenized continuum, whereas the scale one power is written in terms of the discrete bond energies within the DNS region Ω^1 . The variational internal power density at any position can now be written in terms of a sum over the virtual atoms:

$$\delta p_{\text{int}}^1(\mathbf{u}^1) = \frac{\partial \phi_\rho(\mathbf{u}^1)}{\partial \mathbf{u}^1} \cdot \delta \mathbf{v}^1 = \sum_{\alpha=1}^4 \frac{\partial \phi_\rho(\mathbf{u}^1)}{\partial \mathbf{u}_\alpha^1} \cdot \delta \mathbf{v}_\alpha^1 \quad (54)$$

where \mathbf{u}_α^1 is the displacement evaluated at the atomic position α . The total variational internal power can now be written as

$$\delta P_{\text{int}}^1 = \int_{\Omega^0} \boldsymbol{\sigma}^0 : \delta \mathbf{L}^0 d\Omega + \int_{\Omega^1} \sum_\alpha \mathbf{f}_\alpha^1 \cdot \delta \mathbf{v}_\alpha^1 d\Omega \quad (55)$$

where

$$\mathbf{f}_\alpha^1 = \frac{\partial \phi_\rho(\mathbf{u}^1)}{\partial \mathbf{u}_\alpha^1} \quad (56)$$

In the hierarchical approach, the variational internal power is:

$$\delta p_{\text{int}}^1 = \int_{\Omega} \boldsymbol{\sigma}^0 : \delta \mathbf{L}^0 \, d\Omega + \int_{\Omega^1} \sum_{\alpha} \mathbf{f}_{\alpha}^1 \cdot \delta \tilde{\mathbf{v}}_{\alpha}^1 \, d\Omega \quad (57)$$

where $\tilde{\mathbf{v}}_{\alpha}^1$ is the relative velocity at scale 1 evaluated at the VAC atomic position α . We see that Equation (57) provides a mixed representation in that it adopts both continuum and atomistic measures. Once this term is formulated, it replaces the corresponding in the virtual internal power in Equation (44). The MRCT based on VAC model has been implemented in [91]. It has been shown that the model provides a consistent link between the continuum and atomistic representation.

4.7. Stochastic multiresolution continuum analysis

In this section, we outline a new aspect of the multiresolution continuum analysis that is implemented through integration with stochastic analysis. Stochastic multiscale analysis is needed to assess the behavior of material from a point of view that accounts for the inherently random nature in material microstructure, which has a direct influence on material constitutive relations and therefore material performance. In particular, a microheterogeneous material that may appear homogenous at the macroscale contains local heterogeneity that has a significant impact on material behavior such as stress distribution, crack propagation path, and failure. A possible procedure of stochastic multiresolution continuum analysis [92] is presented in Figure 20. The key feature is the establishment of ‘equivalent’ stochastic constitutive relations to replace the expensive DNS of statistical cell models. To account for the randomness in the microstructure, samples of RVE cell model are first generated based on the statistical characterization of the material microstructure. For each sample of RVE cell model, parameters ($\boldsymbol{\theta}^n$) of constitutive models at different scale levels n are identified (calibrated) by fitting the selected constitutive model to match with the simulation results. During this process, the average stress ($\boldsymbol{\sigma}$) and strain measure (\mathbf{L}) associated with the deforming RVE are used to curve-fit a macroscopic constitutive model. To evaluate microscope constitutive relations, the RVE model is examined to first identify regions where the deformation is strongly inhomogeneous. Inhomogeneous deformation generally arises due to the interactions between the microstructural features. A relative strain measure ($\mathbf{L}^n - \mathbf{L}$) is computed as the difference between the average strain in the inhomogeneously deforming region and the average RVE strain. The microstress field ($\boldsymbol{\beta}^n$) within the inhomogeneous averaging volume is then computed via a power equivalence relationship as introduced in Section 4.3. This field is averaged over the inhomogeneous averaging volume to find the continuum microstress. Next, the relationship between the relative strain and continuum microstress is curve-fitted to the chosen constitutive model. The average microstress moment ($\bar{\boldsymbol{\beta}}^n$) is computed within the inhomogeneous averaging volume. The relationship between the strain gradient and microstress moment is then curve-fitted to an appropriate constitutive model. The proceeding steps are repeated for each sample of RVE cell model. The calibrated parameters ($\boldsymbol{\theta}^n$) in the constitutive models obtained based on all samples of the RVE cell model are then used to estimate the statistics and distribution of each parameter $\boldsymbol{\theta}$ as well as their correlations. Finally, the stochastic constitutive relations will be predicted based on the chosen constitutive models and the statistical descriptions of all $\boldsymbol{\theta}^n$.

As demonstrated in [29], correlations of constitutive parameters $\boldsymbol{\theta}^n$ often cannot be ignored due to the strong correlations of material properties, e.g. a porous steel alloy with a large ultimate tensile strength S_{uts} also undergoes a high coalescence stress S_{coal} as shown in Figure 21(a). By considering the correlations of material properties in the form of the correlations of constitutive

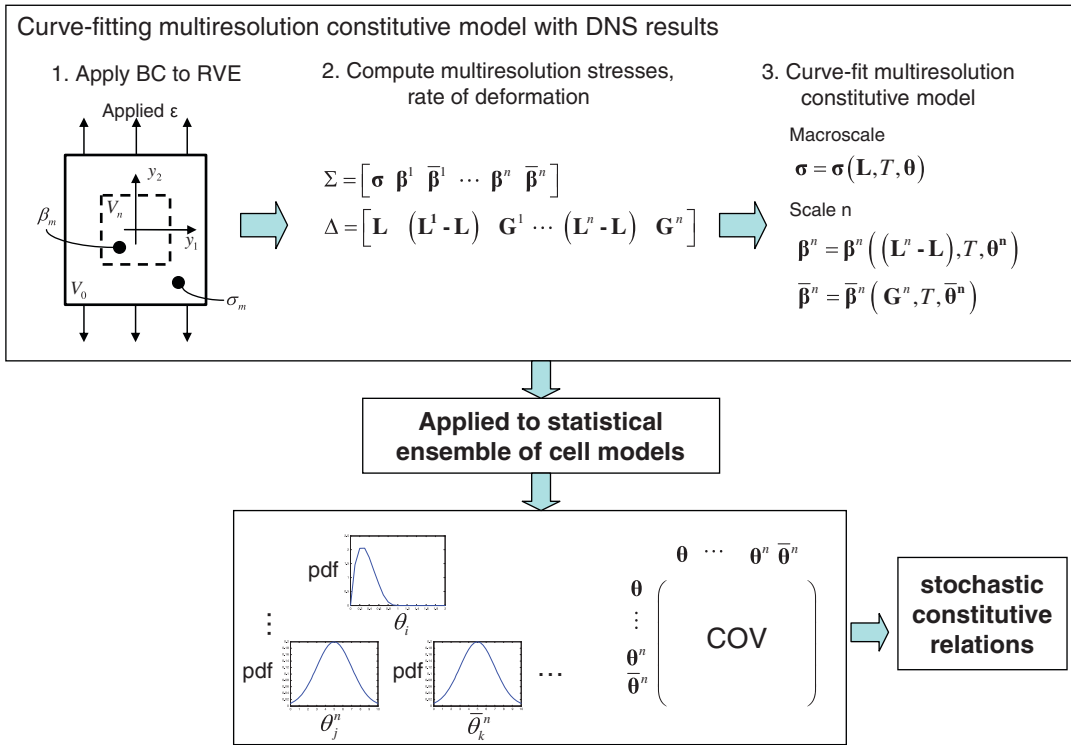


Figure 20. Stochastic calibration of multiscale constitutive models using DNS of statistical cell models.

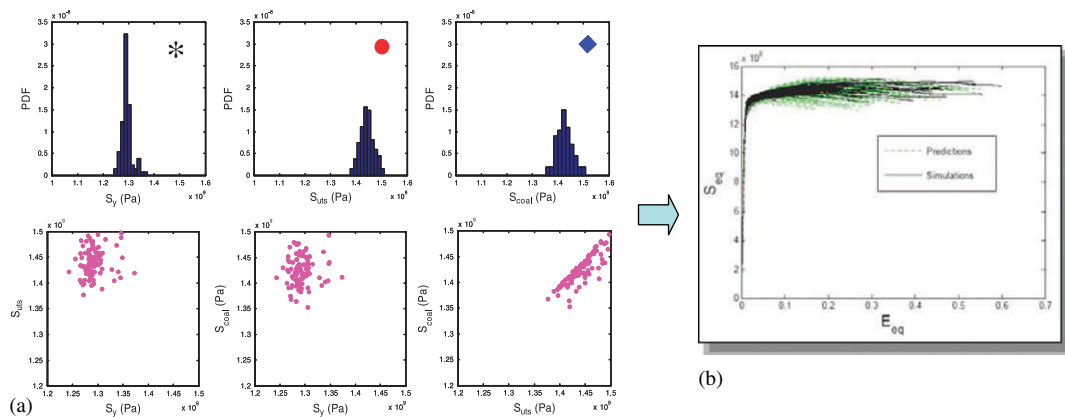


Figure 21. Demonstrative example of stochastic constitutive relation. (Reprinted from [29], copyright 2008, with permission from Elsevier.)

parameters θ , it shows in Figure 21(b) that the predicted set of (stochastic) constitutive relations matches very well with the RVE simulation results.

Statistical analysis and representation of the correlated constitutive parameters is not a trivial task because most of the existing methods only consider the first-order marginal probability density function (PDF) and the pairwise correlation [29]. When a high-order joint marginal PDF needs to be used for characterizing the uncertainty associated with a set of stress–strain curves, alternative uncertainty representation methods such as the polynomial chaos expansion [93] and the Copula method [94–96] can be considered. Our recent study [97] demonstrated the pros and cons of these alternative techniques for capturing high correlations considering both accuracy and ease of implementation.

5. COUPLING WITH QUANTUM MECHANICAL SIMULATIONS

The importance of employing the quantum-mechanical description for resolving the nanomechanics has long been realized by the computational mechanics community. We start our discussion by first introducing Dirac's notation of the wave function, i.e. $\langle\Psi|$ and $|\Psi\rangle$, which are referred to as the 'bra' and 'ket' symbols, respectively. They shall satisfy

$$\langle\Psi|\Psi\rangle = \int \Psi^* \Psi dV = \int |\Psi|^2 dV = 1 \quad \text{and} \quad \langle\Psi|H|\Psi\rangle = \int \Psi^* H \Psi dV \quad (58)$$

in which superscript $*$ gives the complex conjugate, and H is typically the Hamiltonian (total energy) operator for the specific system. $|\Psi|^2$ in Equation (58) gives the PDF for finding the corresponding particle in space. Based on Dirac's notation, the Schrödinger equation for a system is given as

$$H|\Psi\rangle = \varepsilon|\Psi\rangle \quad (59)$$

in which the Hamiltonian operator is $H = -(\hbar/2m)\nabla^2 + U$ with \hbar being Planck's constant divided by 2π , m the particle mass, ∇ the gradient operator (this first term denotes the kinetic energy operator) and U the potential energy function/operator. The major task of the computation is then to solve the eigenvalue problem in Equation (58) for eigenvalues ε and eigenfunctions $|\Psi\rangle$.

A comprehensive review on the techniques and related references for solving the Schrödinger equation can be found in [4, 60, 98]. In this section, we focus on outlining the recent efforts in coupling the quantum-mechanical methods with other coarse-grained approaches. We have excluded many methods that are developed to accelerate the computational speed by developing parameterized empirical models through tight-binding or molecular dynamics due to our limited scope. There are also large amount of work on using FEM shape functions as basis for *ab initio* calculations. We refer to [60, 99, 100] for in-depth discussions and some of the recent development using enrichment approximations based on extended FEM can be found in [101]. Our focus in this section will be on the coupling between the numerical solution to the Schrödinger equation and other modeling and simulation schemes that are developed in the context of continuum mechanics. We note that there are more variety and flexibility in developing the coupling approach because of the additional consideration of the electronic degree of freedom. In the following, we first present several methodologies and then we will discuss our efforts in developing a multiscale concurrent approach.

5.1. An overview of methods of quantum-mechanical coupling

Abraham *et al.* [10, 102] have implemented a direct coupling approach in which the FE, molecular dynamics, and tight-binding methods were performed simultaneously. Because of the differences in the length scale and the details of the solution they obtain, each simulation was performed on a different region of the domain, with a coupling imposed in ‘handshake’ regions where the different simulations overlapped. A classic example is the simulation of the crack propagation in brittle material [102]. The rationale for using a semi-empirical quantum mechanical-based method such as the Tight Binding (TB) approach is for modeling the debonding process that leads to the initiation and propagation of the crack. Hence, TB was implemented at the crack, and the MD was used near the crack surface. The surrounding medium away from this region was treated with FE. The interface between TB and MD, and MD and FE was implemented through a hand-shake scheme. This method has also been used by Nakano *et al.* in large-scale simulations of fracture [103]. Rafii-Tabar *et al.* [104, 105] have presented a related method combining FE and MD for the simulation of crack propagation. A further development that is along the same line is the coarse-grained molecular dynamics [106, 107].

Gavini *et al.* [108–110] have integrated the QC method with the orbital-free density functional theory. The method, which was referred to as QC/OFDFT approach, inherited some of the basic features of the QC method in terms of ability to transitioning between coarse and fine scale representations. An important extension made in this implementation was the coarse-graining of the quantum-mechanical OFDFT description. The variational principal was formulated in which the energy functional was minimized with respect to the square root of the electronic density and nuclei positions. Therefore, the method was aimed at resolving the ground state electron density and equilibrium configuration. Owing to the fact that the method is not limited to the periodical boundary conditions, the quantum-mechanical calculations are performed in the real space. Recent application of this approach can be seen in [111, 112].

The QC implementation of the OFDFT method employed a real-space technique and does not rely on the periodicity assumption. On the other hand, the solution to the Schrodinger equation for a periodical solid can also be of interest in a general context. Such a solution procedure usually involves the use of Bloch’s theorem that takes into account the periodicity and leads to the calculation of the electronic structure that is confined to a representative unit cell. From the application point of view, it is desirable to *directly* built a coarse-grained material/structure model based on such representation, which serves as a link to the underlying *ab initio* models for the general analysis that are governed by electron-mechanical coupling effects. Use of such an approach is well justified by the concurrent nature of the coupling between mechanical deformation and electrons, as well as the important features that go beyond the descriptions by phenomenological or empirical-based approaches. Examples include non-convexity, non-linear elastic effect, and complex energy landscape, etc.

5.2. A multiscale concurrent approach to electron-mechanical coupling

While most of the *ab initio* analysis based on Bloch’s theorem is carried out on the undeformed configuration, extension of this to a deformed configuration can be made if the local homogeneous deformation, or equivalently the Cauchy–Born hypothesis still holds. Under this assumption, one can show that the periodic arrangement of the lattice is preserved in the local sense. One could, therefore, extract a local representation of the unit cell upon which the quantum-mechanical calculation will be performed. These calculations are usually performed in the wave number space

as it produces the band structure and Density of States that are important for evaluating the physical properties. As the size of the unit cell is much smaller than that of a global problem and involves much less number of degrees of freedom for the electrons, the computational saving achieved from the periodical assumption is thus enormous. More substantial savings can be achieved by combining this with FEM calculations.

Earlier development along this direction yields a hyperelastic model by introducing the dependence of the potential energy density functional on the deformation gradient. For instance, Tadmor and colleagues [113] have integrated the TB approach with QC model and focused on the mechanical analysis of complex crystals such as Silicon. Their model also included the inner displacement effect. The use of TB model rather than an empirical potential is justified by its ability to eliminate the non-physical local minimum resolved from the latter. By solving a continuum crystal elasticity model [114] derived from the Tersoff–Brenner potential, Liu *et al.* [115] studied the influence of mechanical deformations on the electronic properties of CNTs using the TB approach. They have reported interesting transition between metallic and semi-conducting behavior in CNT structures when tension or twist is introduced. A further study of electrical transport for deformed CNT using the same model was discussed by Johnson *et al.* [116]. The works by Liu *et al.* [115] and Johnson *et al.* [116] have focused on solving multi-physics constitutive equations.

A multiscale concurrent approach was recently proposed by Qian *et al.* [22]. In this approach, the tight-binding approach was integrated with the virtual atom cluster model developed earlier. An important distinction compared with the earlier approach was that the Cauchy–Born hypothesis was not introduced and correspondingly no stress–strain relation was being evaluated. The information passage between the TB and FEM (or meshfree) calculation was carried out directly through the VAC model. The implementation enabled the use of existing TB and FEM packages without much modification. The specific implementation is discussed in the following.

5.2.1. An introduction to the tight-binding method. As a semi-empirical approach, the tight-binding method expresses the solution to the i th eigenfunction $|\Psi_i\rangle$ as a linear combination of the basis functions, i.e.

$$|\Psi_i\rangle = \sum_{j=1}^{n_e} c_{ij} |\psi_j\rangle = \{c\}_i^T \{|\psi\rangle\} = \mathbf{c}_i^T \{|\psi\rangle\} \quad (60)$$

in which n_e is the number of base functions, c_{ij} is the linear coefficient to be determined and $|\psi_j\rangle$ is the corresponding j th base function with j ranging from 1 to n_e . The choice of the basis function is typically from the so-called one-electron solutions. Based on this, the Schrödinger equation becomes

$$H \sum_{j=1}^{n_e} c_{ij} |\psi_j\rangle = \varepsilon_i \sum_{j=1}^{n_e} c_{ij} |\psi_j\rangle \quad (61)$$

Following the variational principle, Equation (61) is pre-multiplied by the base function $\langle\psi_{j'}|$ for $j' = 1, \dots, n_e$. For each j' ,

$$\langle\psi_{j'}| H \sum_{j=1}^{n_e} c_{ij} |\psi_j\rangle = \varepsilon_i \langle\psi_{j'}| \sum_{j=1}^{n_e} c_{ij} |\psi_j\rangle \quad (62)$$

We define $H_{j'j} = \langle \psi_{j'} | H | \psi_j \rangle$ and $S_{j'j} = \langle \psi_{j'} | \psi_j \rangle$, Equation (10) can be rewritten as:

$$\sum_{j=1}^{n_e} H_{j'j} c_{ij} = \varepsilon_i \sum_{j=1}^{n_e} S_{j'j} c_{ij} \quad (63)$$

Generalizing Equation (63) for all the choices of j' leads to eigenvalue problem

$$\hat{H} \mathbf{c}_i = \varepsilon_i \mathbf{S} \mathbf{c}_i \quad (64)$$

in which \hat{H} is called the transfer integral or Hamiltonian matrix with element $H_{j'j}$ and \mathbf{S} is called an overlap integral matrix with element $S_{j'j}$. In the tight-binding method, the transfer and hopping integrals are evaluated using empirical forms. The eigenvector \mathbf{c}_i contains all the linear coefficients c_{ij} to be solved for the i th eigenvalue. The computational cost in solving the eigenvalue problem is on the order of $O(n_e^3)$ in which n_e is the total number of electronic basis functions used, thus it is computationally intensive.

5.2.2. The multiscale concurrent model based on VAC. For nanocrystals that demonstrate periodicities in the lattice structure, the computational cost associated with solving Equation (64) can be greatly reduced by employing the Bloch theorem [117]. Based on this theorem, the base solution to the Schrödinger equation for a periodic potential can be expressed as the product of a plane wave $e^{i\mathbf{k}\cdot\mathbf{r}}$ with a function that has the periodicity of the lattice. (For detailed proof, see Kittel [118].) Here the wave vector \mathbf{k} is related to the periodicity of the unit cell for a particular problem. Using i as the index of atom within the unit cell and α as the index for orbital, we express the basis as:

$$|\psi_{i\alpha}(\mathbf{k}, \mathbf{r})\rangle = \frac{1}{\sqrt{N_{\text{cell}}}} \sum_I e^{i\mathbf{k}\cdot(\mathbf{R}_I + \boldsymbol{\eta}_i)} |\phi_\alpha(\mathbf{r} - \mathbf{R}_I - \boldsymbol{\eta}_i)\rangle \quad (65)$$

Here $|\phi_\alpha\rangle$ is the one-electron base function, \mathbf{k} is the wave vector, N_{cell} is the number of the translational unit cells, \mathbf{R}_I is the coordinate of the I th unit cell, $\boldsymbol{\eta}_i$ is the position of the i th atom within the unit cell and \mathbf{r} is the spatial coordinate upon which the base function $|\phi_\alpha\rangle$ is being evaluated. The exponential function reflects the periodicity argument from the Bloch theorem.

The TB approximation is now

$$|\Psi(\mathbf{k}, \mathbf{r})\rangle = \sum_{i\alpha} C_{i\alpha} |\psi_{i\alpha}(\mathbf{k}, \mathbf{r})\rangle \quad (66)$$

Following the same variational principle, we derive the eigenvalue problem

$$\langle \psi_{j\beta}(\mathbf{k}, \mathbf{r}) | H \sum_{i\alpha} C_{i\alpha} |\psi_{i\alpha}(\mathbf{k}, \mathbf{r})\rangle = \varepsilon \langle \psi_{j\beta}(\mathbf{k}, \mathbf{r}) | \sum_{i\alpha} C_{i\alpha} |\psi_{i\alpha}(\mathbf{k}, \mathbf{r})\rangle \quad (67)$$

and secular equation for determining the linear coefficients

$$\langle \psi_{j\beta}(\mathbf{k}, \mathbf{r}) | H | \psi_{i\alpha}(\mathbf{k}, \mathbf{r})\rangle - \varepsilon \langle \psi_{j\beta}(\mathbf{k}, \mathbf{r}) | \psi_{i\alpha}(\mathbf{k}, \mathbf{r})\rangle = 0 \quad (68)$$

The size of the eigenvalue problem associated with Equation (68) can be greatly reduced by invoking Bloch's theorem. First of all, Equation (68) will be sparse and banded due to the fact that the interaction will be limited to the nearest neighbor. With Bloch's approximation, it can be shown at the base orbitals for different atoms will be the same as if they are in the same symmetry group. The combination of these two properties leads to a block diagonal matrix from Equation (68).

Instead of solving the original eigenvalue problem associated with a global matrix, the final matrix size for the reduced problem corresponds to the total number of electronic wave base functions that are involved in the unit cell. For problem involving CNT, we have incorporated the helical symmetry in the approximation of the base and have used the sp^3 orthogonal tight-binding model. This leads to an 8×8 matrix being solved for the eigenvalue problem.

Once the eigenvalue problem is solved, we have $|\Psi^{(l)}(\mathbf{k}, \mathbf{r})\rangle = \sum_{i\alpha} C_{i\alpha}^{(l)} |\psi_{i\alpha}(\mathbf{k}, \mathbf{r})\rangle$ with $\varepsilon^{(l)}$ being the l th eigenvalue and $C_{i\alpha}^{(l)}$ the eigenvector. We then evaluate the potential energy of the i th atom in the unit cell as

$$\phi_i = \frac{1}{2} \sum_j \left[2 \sum_k \sum_{l=1}^{\text{HOMO}} \langle \Psi^{(l)}(\mathbf{k}, \mathbf{r}) | H(r_{ij}) | \Psi^{(l)}(\mathbf{k}, \mathbf{r}) \rangle + E^{\text{ion}}(r_{ij}) \right] \quad (69)$$

in which HOMO stands for the highest occupied molecular orbital. The factor of 2 comes from the Pauli exclusion principle and $\frac{1}{2}$ from the splitting of the bonding energy. The term E^{ion} represents the effect due to ion-ion repulsion and is expressed in an empirical form.

From Equation (69), it can be seen that one also needs to obtain the derivative of the total energy with respect to the spatial coordinates, in order to resolve the electron-mechanical coupling using the VAC model. The contribution from the TB model is obtained by further applying the Hellmann-Feynman theorem [119],

$$\frac{\partial \phi_i}{\partial \mathbf{x}} = \frac{1}{2} \sum_j \left[2 \sum_{\mathbf{k}} \sum_{l=1}^{\text{HOMO}} \left\langle \Psi^{(l)} \left| \frac{\partial H(\mathbf{r}_{ij})}{\partial \mathbf{x}} \right| \Psi^{(l)} \right\rangle + \frac{\partial E^{\text{ion}}(\mathbf{r}_{ij})}{\partial \mathbf{x}} \right] \quad (70)$$

For the l th eigenvalue,

$$\langle \Psi^{(l)} | H(\mathbf{r}_{ij}) | \Psi^{(l)} \rangle = \frac{1}{N} \begin{pmatrix} C_{i,s}^* \\ C_{i,x}^* \\ C_{i,y}^* \\ C_{i,z}^* \end{pmatrix}^T T_i H_{ij} T_j^T \begin{pmatrix} C_{j,s} \\ C_{j,x} \\ C_{j,y} \\ C_{j,z} \end{pmatrix} \cdot e^{i\mathbf{k} \cdot (\mathbf{R}_K + \boldsymbol{\eta}_l)} \quad (71)$$

in which $\{C_{i,s} C_{i,x} C_{i,y} C_{i,z}\}$ and $\{C_{j,s} C_{j,x} C_{j,y} C_{j,z}\}$ are l th eigenvectors and superscript * gives their complex conjugate.

Once the potential energy and inter-atomic force are resolved, the implementation of the VAC model is the same as outlined earlier. Detailed implementation is described in [22].

In the following, we demonstrate the application of the multiscale concurrent model for analyzing the electron-mechanical coupling in CNT structures. Based on the chiral index (n, m) , we consider three types of CNTs: zigzag ($m = 0$), armchair ($n = m$) and chiral (not zigzag or armchair). Detailed structure definition based on chiral index can be seen in [98]. Figure 22(a) illustrates the coupling based on VAC in which the original molecular structure is replaced using meshfree representation [120]. All the tubes are fully relaxed and then are subjected to tension or bending. The loads are applied incrementally so that at each step we are able to resolve the electronic band structure and extract the corresponding electronic properties.

For tension, a linear relation between the band gap E_g and applied tensile strain is observed in all the tube from Figure 22(b). From the theoretical analysis based on zone-folding approach, it is known that $E_g = 0$ if $\text{mod}(n - m, 3) = 0$ at zero strain. However, our simulation shows that this

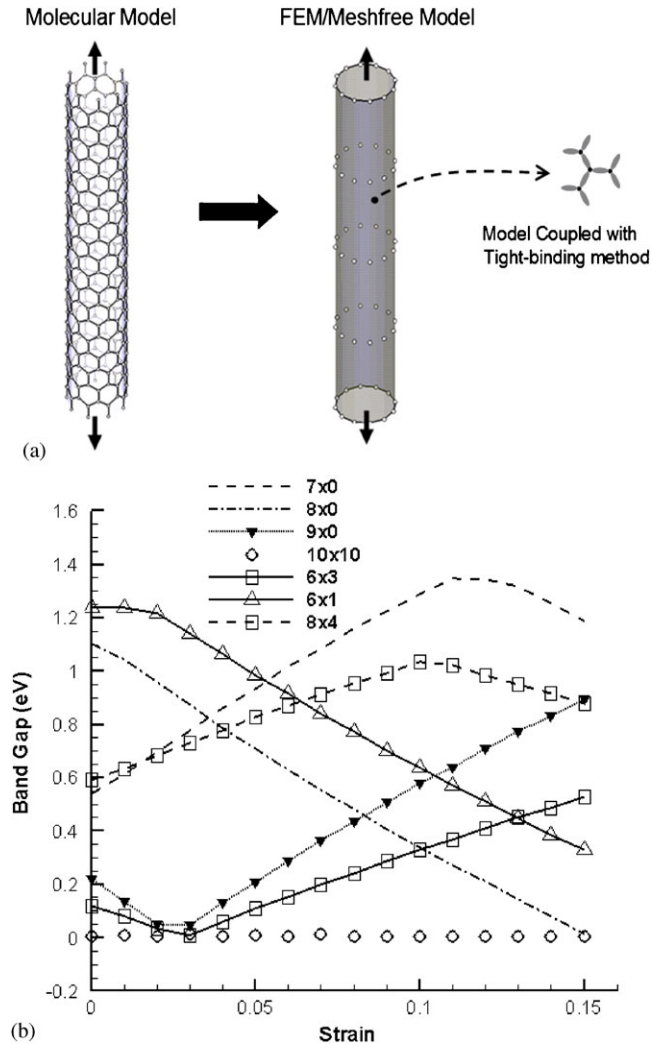


Figure 22. (a) From molecular model to FEM/Meshfree model using VAC and (b) computed band gap as a function of the tensile strain for a number of single-walled CNTs.

is not the case for tube with small radius, e.g. finite band gap is observed in (9,0) and (6,3) as shown. These are the indications of effects of curvature-induced relaxation and rehybridization. The armchair tube, on the other hand, retains a zero band gap at all strains. This is due to the fact that the symmetry properties of the armchair tube are not altered by the applied tension and therefore it remains metallic under deformation. At finite strain, we see that the change in the band gap is not trivial for all the tubes. In particular, we observe the switch between a finite band gap and zero band gap, such as those in (8,0), (9,0) and (8,4) tubes. This is an indication that these tubes could switch from semi-conducting to metallic or vice versa by simply applying tension. The electron-mechanical coupling and sensitivity revealed from this model is significant for applications such as sensors and actuators.

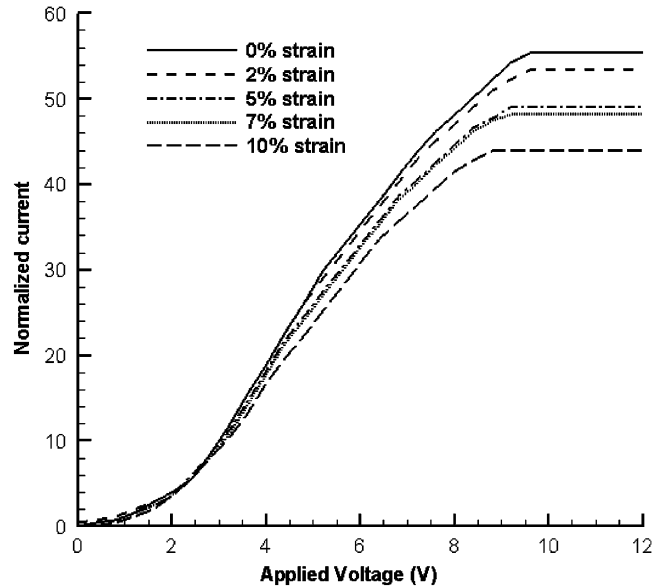


Figure 23. The I-V relation for a (9,0) tube at different tensile strains.

The electric transport properties can be computed from the electronic band structures at different tensile strains. In Figure 23, we plotted the I-V curve that is derived from the Landauer–Buttiker’s formula [121]. The currents plotted are in the unit of 77.48×10^{-6} A. We see that at small voltage (<4 V), the I-V curve is not sensitive to the tensile strain. Large discrepancies are observed, however, at large strains. Overall, the applied tension reduces conductivity. At high strain values, we see that the values of the current seem to be converging to a constant. This is an indication on the saturation of the available conducting channel. The specific saturation current is dependent on the chiral index.

We proceed to look at the effect of the bending deformation. Five tubes with different types of chirality indices are considered, i.e. (10,10), (9,0), (10,0), (12,3), and (10,5). An incremental bending angle of 0.25° per step is imposed on each side until a final bending of 10° is reached (Figure 24 shows the bending deformation for a (10,0) tube.). We chose a sensitivity index, which is obtained by dividing the band gap change by the incremental bending angle. For all the five tubes tested, we find that this sensitivity index is less than 0.05 eV/degree. We further illustrate using (9,0) tube as an example. We show in Figure 25 the I-V curves obtained at zero bending and 20° total bending angle. The two curves essentially overlap. The difference between the two is plotted as a solid line, which shows a very little difference. This low sensitivity indicates that the bending has little effect on the electronic structures.

6. CONCLUSIONS

We have presented an overview of multiscale models for complex material systems with a special emphasis on the link between quantum-mechanical model to multiscale statistical continuum model.



Figure 24. The bending deformation in a (10,0) tube resolved from the multiscale concurrent model.

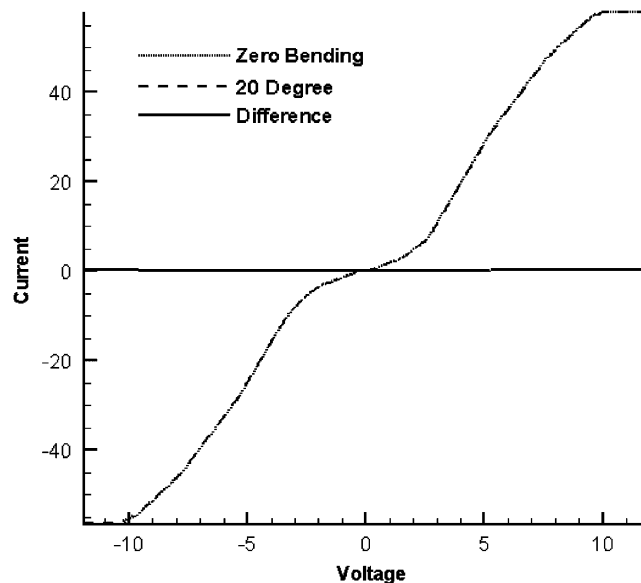


Figure 25. The I-V curve for a (9,0) tube at different bending angles.

Compared with many of the other methods that have been developed, we show the unique advantage of the bridging scale concept, which enables effective separation of the physical variables that are defined at their relative spatial and time scales. This also leads to a unique decomposition of the momentum and energy representations and serves as a stepping stone to some of the extensions described in this paper.

Several applications of the BSM have been presented. First, we have discussed the application of the bridging scale concept in the modeling of wave and dynamic crack propagation. We have shown that the spurious effect associated with wave-reflecting boundary conditions can be effectively eliminated in the simulation of crack growth and branching. An extension aimed at integrating this concept with a space-time formulation has also been demonstrated. This effectively provides a framework for dealing with multiscale phenomena in both spatial and temporal domain. The ability of this approach to achieve non-reflective and wave-transmitting boundary condition is illustrated. Another important extension is made to apply the bridging scale decomposition to non-equilibrium

phenomena. We have shown that this method is more reliable in its ability to capture thermally activated shock waves or dislocations in comparison with the conventional molecular dynamics.

We then focused on the MRCT, based on a multiscale virtual power decomposition. A length scale is associated with the definition of the virtual power terms at each scale. As a result, a set of multiresolution governing equations can be derived that reflect the average response as well as the inhomogeneous effects. The application of this methodology has been illustrated through the analysis of adiabatic shear band and fracture in high-strength steel. We have further shown that a non-local representation based on the virtual atom cluster model can also be introduced for multiresolution of heterogeneous materials. While the procedure is similar, a key difference is the non-local representation of the cluster model and therefore the intrinsic length scale is already built-in. Motivated by the random nature of the material structure, we have shown an extension of this approach, by incorporating statistic analysis in the multiresolution continuum model. This has been implemented by establishing equivalent stochastic constitutive models as an alternative to the DNS approach, which can be very expensive. This methodology allows establishing a link between the correlation of the material properties and the stochastic nature of the constitutive behavior.

Finally, we have discussed the development of a coarse-grained quantum-mechanical model aimed at predicting the electron-mechanical coupling in nanostructured materials, whereas achieving significant reduction in the computational expense through the introduction of a local model. Using CNT as an example, we have shown that the sensitivity of the electronic structure is highly dependent upon the deformation mode. In certain cases, an interesting switch between semi-conducting and metallic behavior has been observed.

In conclusion, recent efforts in developing multiscale methods based on the bridging scale concepts have been presented. The overview on the approaches aiming at linking multiple spatial and temporal scales has shed new lights on a number of important applications in the field of nanomechanics. Nevertheless, building a truly seamless design environment is still an open subject with many questions that remain to be answered. While it is not surprising that the topics of mechanics have been frequently brought up in many nanotechnology applications, there is increasing consensus that studying these topics will unavoidably involve other disciplines. Some of the applications presented in this paper clearly show this trend and demonstrate the importance of understanding these phenomena and the related mechanisms at different levels.

ACKNOWLEDGEMENTS

WKL acknowledges the support from the National Science Foundation (CMMI-0823327) and Army Research Lab, ONR/DAPRA D3D project, and DoE (Sandia national Lab); and Sections 3.1–3.3 are completed under the support of the World Class University program (R33-10079) under the Ministry of Education, Science and Technology, Republic of Korea. DQ and SC acknowledge the general support from National Science Foundation (CMMI-0600583 and -0700107). SL was supported by a grant from NSF (CMS-0239130), which is greatly appreciated. WC acknowledges the grant support from National Science Foundation (CMMI – 0522662). Any opinions, findings, conclusions, or recommendations expressed in these documents are those of the author(s) and do not necessarily reflect the views of the National Science Foundation.

REFERENCES

1. Schiff LI. *Quantum Mechanics*. McGraw-Hill: New York, 1968.
2. Liu WK, Karpov EG, Park HS. *Nano Mechanics and Materials: Theory, Multiscale Methods and Applications*. Wiley: New York, 2006.

3. Hao S, Liu WK, Chang CT. Computer implementation of damage models by finite element and meshfree methods. *Computer Methods in Applied Mechanics and Engineering* 2000; **187**:401–440.
4. Liu WK, Jun S, Qian D. Computational nanomechanics of materials. *Journal of Computational and Theoretical Nanoscience* 2008; **5**(5):970–996.
5. Zhou SJ, Lomdahl PS, Thomson R, Holian BL. Dynamic crack processes via molecular dynamics. *Physical Review Letters* 1996; **76**(13):2318–2321.
6. Zhang S, Mielke SL, Khare R, Troya D, Ruoff RS, Schatz GC, Belytschko T. Mechanics of defects in carbon nanotubes: atomistic and multiscale simulations. *Physical Review B* 2005; **71**(11):540301–540312.
7. Arroyo M, Belytschko T. An atomistic-based membrane for crystalline films one atom thick. *Journal of Mechanics and Physics of Solids* 2002; **50**:1941–1977.
8. Belytschko T, Xiao SP, Schatz GC, Ruoff RS. Atomistic simulations of nanotube fracture. *Physical Review B* 2002; **65**(23):543001–543008.
9. Mura T. *Micromechanics of Defects in Solids*. Kluwer: Dordrecht, 1991.
10. Broughton JQ, Abraham FF, Bernstein N, Kaxiras E. Concurrent coupling of length scales: methodology and application. *Physical Review B* 1999; **60**(4):2391–2403.
11. Fish J, Wen J. Discrete-to-continuum bridging based on multigrid principles. *Computer Methods in Applied Mechanics and Engineering* 2004; **193**:1693–1711.
12. Karpov EG, Wagner GJ, Liu WK. A Green's function approach to deriving non-reflecting boundary conditions in molecular dynamics simulations. *International Journal for Numerical Methods in Engineering* 2005; **62**:1250–1262.
13. Knap J, Ortiz M. An analysis of the quasicontinuum method. *Journal of the Mechanics and Physics of Solids* 2001; **49**(9):1899–1923.
14. Park HS, Karpov EG, Klein PA, Liu WK. Three-dimensional bridging scale analysis of dynamic fracture. *Journal of Computational Physics* 2005; **207**(2):588–609.
15. Park HS, Karpov EG, Liu WK, Klein PA. The bridging scale for two-dimensional atomistic/continuum coupling. *Philosophical Magazine* 2005; **85**(1):79–113.
16. Park HS, Liu WK. An introduction and tutorial on multiple-scale analysis in solids. *Computer Methods in Applied Mechanics and Engineering* 2004; **193**(17–20):1733–1772.
17. Bauman PT, Oden JT, Prudhomme S. Adaptive multiscale modeling of polymeric materials with Arlequin coupling and goals algorithms. *Computer Methods in Applied Mechanics and Engineering* 2009; **198**(5–8):799–818.
18. Hawkins A, Oden JT. Toward a predictive model of tumor growth. *ICES Report*, The university of Texas at Austin, 2008.
19. Xiao SP, Belytschko T. A bridging domain method for coupling continua with molecular dynamics. *Computer Methods in Applied Mechanics and Engineering* 2004; **193**(17–20):1645–1669.
20. Xu M, Belytschko T. Conservation properties of the bridging domain method for coupled molecular/continuum dynamics. *International Journal for Numerical Methods in Engineering* 2008; **76**(3):278–294.
21. Qian D, Wagner GJ, Liu WK. A multiscale projection method for the analysis of carbon nanotubes. *Computer Methods in Applied Mechanics and Engineering* 2004; **193**(17–20):1603–1632.
22. Qian D, Liu WK, Zheng QJ. Concurrent quantum/continuum coupling analysis of nanostructures. *Computer Methods in Applied Mechanics and Engineering* 2008; **197**(41–42):3291–3323.
23. Gao HJ, Huang Y, Nix WD, Hutchinson JW. Mechanism-based strain gradient theory—I. Theory. *Journal of the Mechanics and Physics of Solids* 1999; **47**:1239–1263.
24. Huang Y, Gao HJ, Nix WD, Hutchinson JW. Mechanism-based strain gradient theory—II. Analysis. *Journal of the Mechanics and Physics of Solids* 2000; **48**:99–128.
25. Fleck N, Muler GM, Ashby MF, Hutchinson JW. Strain gradient plasticity: theory and experiment. *Acta Metallurgy and Materials* 1994; **42**:475–487.
26. Kadowaki H, Liu WK. Bridging multiscale method for localization problems. *Computer Methods in Applied Mechanics and Engineering* 2004; **193**:3267–3302.
27. Mindlin RD. Microstructure in linear elasticity. *Archive for Rational Mechanics and Analysis* 1964; **16**:15–78.
28. McVeigh C, Vernerey F, Liu WK, Brinson LC. Multiresolution analysis for material design. *Computer Methods in Applied Mechanics and Engineering* 2006; **195**(37–40):5053–5076.
29. Yin X, Chen W, To AC, McVeigh C, Liu WK. Statistical volume element method for predicting microstructure-constitutive property relations. *Computer Methods in Applied Mechanics and Engineering* 2008; **197**(43–44):3516–3529.

30. Yin X, Lee S, Chen W, Liu WK. Efficient random field uncertainty propagation in design using multiscale analysis. *ASME Journal of Mechanical Design* 2009; **131**(2):021006.
31. Alzebedeh K, Al-Ostaz A, Jasiuk I, Ostoja-Starzewski M. Fracture of random matrix-inclusion composites: scale effects and statistics. *International Journal of Solids and Structures* 1998; **35**(19):2537–2566.
32. Arnst M, Ghanem RG. Probabilistic equivalence and stochastic model reduction in multiscale analysis. *Computer Methods in Applied Mechanics and Engineering* 2008; **197**(43–44):3584–3592.
33. Xu XF. A multiscale stochastic finite element method on elliptic problems involving uncertainties. *Computer Methods in Applied Mechanics and Engineering* 2007; **196**(25–28):2723–2736.
34. Charnpris DC, Schueller GI, Pellissetti MF. The need to linking micromechanics of materials with stochastic finite elements: a challenge for materials science. *Computational Materials Science* 2007; **41**(1):27–37.
35. Vernerey F, Liu WK, Moran B. Multi-scale micromorphic theory for hierarchical materials. *Journal of the Mechanics and Physics of Solids* 2007; **55**(12):2603–2651.
36. Vernerey FJ, Liu WK, Moran B, Olson G. A micromorphic model for the multiple scale failure of heterogeneous materials. *Journal of the Mechanics and Physics of Solids* 2008; **56**(4):1320–1347.
37. McVeigh C, Liu WK. Linking microstructure and properties through a predictive multiresolution continuum. *Computer Methods in Applied Mechanics and Engineering* 2008; **197**(41–42):3268–3290.
38. McVeigh C, Liu WK. Multiresolution modeling of ductile reinforced brittle composites. *Journal of the Mechanics and Physics of Solids* 2009; **57**(2):244–267.
39. Kohlhoff S, Gumbsch P, Fischmeister HF. Crack-propagation in Bcc crystals studied with a combined finite-element and atomistic model. *Philosophical Magazine A—Physics of Condensed Matter Structure Defects and Mechanical Properties* 1991; **64**(4):851–878.
40. Abraham FF. Dynamics of brittle fracture with variable elasticity. *Physical Review Letters* 1996; **77**(5):869–872.
41. Mullins M, Dokainish MA. Simulation of the (001) plane crack in alpha-iron employing a new boundary scheme. *Philosophical Magazine A* 1982; **46**(5):771–787.
42. Tadmor EB, Ortiz M, Phillips R. Quasicontinuum analysis of defects in solids. *Philosophical Magazine A—Physics of Condensed Matter Structure Defects and Mechanical Properties* 1996; **73**(6):1529–1563.
43. Holian BL, Ravelo R. Fracture simulations using large-scale molecular-dynamics. *Physical Review B* 1995; **51**(17):11275–11288.
44. Berendsen HJC, van Gunsteren WF. In *Dynamics Simulation of Statistical Mechanical Systems*, Ciccotti GPF, Hoover WG (eds), vol. 63. North-Holland: Amsterdam, 1986; 493.
45. Gumbsch P, Zhou SJ, Holian BL. Molecular dynamics investigation of dynamic crack stability. *Physical Review B* 1997; **55**(6):3445–3455.
46. Adelman SA, Doll JD. Generalized Langevin equation approach for atom/solid-surface scattering-collinear atom/harmonic chain model. *Journal of Chemical Physics* 1974; **61**(10):4242–4245.
47. Adelman SA, Doll JD. Generalized Langevin equation approach for atom/solid surface scattering—general formulation for classical scattering of harmonic solids. *Journal of Chemical Physics* 1976; **64**(6):2375–2388.
48. Cai W, de Koning M, Bulatov VV, Yip S. Minimizing boundary reflections in coupled-domain simulations. *Physical Review Letters* 2000; **85**(15):3213–3216.
49. E W, Huang ZY. Matching conditions in atomistic-continuum modeling of materials. *Physical Review Letters* 2001; **97**(13):5501–5504.
50. E W, Huang ZY. A dynamic atomistic-continuum method for the simulation of crystalline material. *Journal of Computational Physics* 2002; **182**:234–261.
51. Wagner GJ, Liu WK. Coupling of atomistic and continuum simulations using a bridging scale decomposition. *Journal of Computational Physics* 2003; **190**(1):249–274.
52. Liu WK, Jun S, Zhang YF. Reproducing Kernel particle methods. *International Journal for Numerical Methods in Fluids* 1995; **20**(8–9):1081–1106.
53. Liu WK, Jun S, Li SF, Adee J, Belytschko T. Reproducing kernel particle methods for structural dynamics. *International Journal for Numerical Methods in Engineering* 1995; **38**(10):1655–1679.
54. Liu WK, Li SF, Belytschko T. Moving least-square reproducing kernel methods. I. Methodology and convergence. *Computer Methods in Applied Mechanics and Engineering* 1997; **143**(1–2):113–154.
55. Gonella S, Ruzzene M. Bridging scales analysis of wave propagation in heterogeneous structures with imperfections. *Wave Motion* 2008; **45**(4):481–497.
56. Tang SQ, Hou TY, Liu WK. A pseudo-spectral multiscale method: interfacial conditions and coarse grid equations. *Journal of Computational Physics* 2006; **213**(1):57–85.
57. Tang SQ, Hou TY, Liu WK. A mathematical framework of the bridging scale method. *International Journal for Numerical Methods in Engineering* 2006; **65**(10):1688–1713.

58. Karpov EG, Park HS, Liu WK. Phonon heat bath for the atomistic and multiscale simulation of solids. *International Journal for Numerical Methods in Engineering* 2007; **70**(3):351–378.
59. Farrell DE, Karpov EG, Liu WK. Algorithms for bridging scale method parameters. *Computational Mechanics* 2007; **40**(6):965–978.
60. Liu WK, Karpov EG, Zhang S, Park HS. An introduction to computational nanomechanics and materials. *Computer Methods in Applied Mechanics and Engineering* 2004; **193**(17–20):1529–1578.
61. Weeks WT. Numerical inversion of Laplace transforms using Laguerre functions. *Journal of the ACM* 1966; **13**(3):419–429.
62. Farrell DE, Park HS, Liu WK. Implementation aspects of the bridging scale method and application to intersonic crack propagation. *International Journal for Numerical Methods in Engineering* 2007; **71**(5):583–605.
63. Crump KS. Numerical inversion of Laplace transforms using a Fourier-series approximation. *Journal of the ACM* 1976; **23**(1):89–96.
64. Chirputkar SU, Qian D. Coupled atomistic/continuum simulation based on extended space–time finite element method. *CMES—Computer Modeling in Engineering and Sciences* 2008; **24**(2–3):185–202.
65. Hulbert GM, Hughes TJR. Space–time finite-element methods for 2nd-order hyperbolic-equations. *Computer Methods in Applied Mechanics and Engineering* 1990; **84**(3):327–348.
66. Li XD, Wiberg NE. Structural dynamic analysis by a time-discontinuous Galerkin finite element method. *International Journal for Numerical Methods in Engineering* 1996; **39**(12):2131–2152.
67. Chessa J, Belytschko T. Arbitrary discontinuities in space–time finite elements by level sets and X-FEM. *International Journal for Numerical Methods in Engineering* 2004; **61**(15):2595–2614.
68. Belytschko T, Black T. Elastic crack growth in finite elements with minimal remeshing. *International Journal for Numerical Methods in Engineering* 1999; **45**(5):601–620.
69. Dolbow J, Moes N, Belytschko T. Modeling fracture in Mindlin–Reissner plates with the extended finite element method. *International Journal of Solids and Structures* 2000; **37**(48–50):7161–7183.
70. Dolbow J, Moes N, Belytschko T. Discontinuous enrichment in finite elements with a partition of unity method. *Finite Elements in Analysis and Design* 2000; **36**(3–4):235–260.
71. Sukumar N, Moes N, Moran B, Belytschko T. Extended finite element method for three-dimensional crack modelling. *International Journal for Numerical Methods in Engineering* 2000; **48**(11):1549–1570.
72. Liu XH, Li S. Non-equilibrium multiscale computation model. *Journal of Chemical Physics* 2007; **126**:124105.
73. Li S, Sheng N, Liu XH. A non-equilibrium multiscale paradigm. *Chemical Physics Letters* 2007; **451**:293–300.
74. Sheng N, Li S. A multiscale non-equilibrium molecular dynamics algorithm and its applications. *International Journal of Applied Mechanics* 2009; **1**(3):1–16.
75. Li S, Sheng N. On multiscale non-equilibrium molecular dynamics simulations (in this Issue). *International Journal for Numerical Methods in Engineering* 2010; DOI: 10.1002/nme.2849.
76. Du Q, Faber V, Gunzburger M. Centroidal Voronoi tessellations: applications and algorithms. *SIAM Review* 1999; **41**(4):637–676.
77. Nose S. An extension of the canonical ensemble molecular-dynamics method. *Molecular Physics* 1986; **57**(1):187–191.
78. Hoover WG. Canonical dynamics—equilibrium phase-space distributions. *Physical Review A* 1985; **31**(3):1695–1697.
79. Nose S. A molecular-dynamics method for simulations in the canonical ensemble. *Molecular Physics* 1984; **52**(2):255–268.
80. Weiner JH. *Statistical Mechanics of Elasticity*. Wiley: New York, 1983.
81. Jiang H, Huang Y, Hwang KC. A finite-temperature continuum theory based on interatomic potentials. *Journal of Engineering Materials and Technology—Transactions of the ASME* 2005; **127**(4):408–416.
82. Kim JH, Liu WK, Lee C. Multi-scale solid oxide fuel cell materials modeling. *Computational Mechanics* 2009; **44**(5):683–703.
83. Hill R. Elastic properties of reinforced solids—some theoretical principles. *Journal of the Mechanics and Physics of Solids* 1963; **11**(5):357–372.
84. Vernerey F, Liu WK, Moran B, Olson G. Multi-length scale micromorphic process zone model. *Computational Mechanics* 2009; **44**(3):433–445.
85. Medyanik SN, Liu WK, Li SF. On criteria for dynamic adiabatic shear band propagation. *Journal of the Mechanics and Physics of Solids* 2007; **55**(7):1439–1461.
86. Wright TW, Walter JW. The asymptotic structure of an adiabatic shear band in antiplane motion. *Journal of the Mechanics and Physics of Solids* 1996; **44**(1):77–97.

87. McVeigh C, Vernerey F, Liu WK, Moran B, Olson G. An interactive micro-void shear localization mechanism in high strength steels. *Journal of the Mechanics and Physics of Solids* 2007; **55**(2):225–244.
88. Siad L, Liu WK, Benabbes A. Explicit numerical study of softening in porous ductile solids. *Mechanics Research Communications* 2009; **36**(2):236–245.
89. Mcveigh C, Liu WK. Multiresolution continuum modeling of micro-void assisted dynamic adiabatic shear band propagation. *Journal of the Mechanics and Physics of Solids* 2010; **58**(2):187–205.
90. Qian D, Gondhalekar RH. A virtual atom cluster approach to the mechanics of nanostructures. *International Journal for Multiscale Computational Engineering* 2004; **2**(2):277–289.
91. Liu WK, McVeigh C. Predictive multiscale theory for design of heterogeneous materials. *Computational Mechanics* 2008; **42**(2):147–170.
92. Liu WK, Larbi S, Tian R, Lee SH, Lee D, Yin X, Chen W, Chan S, Olson GB, Lindgeen LE, Horstemeyer MF, Chang YS, Choi JB, Kim YJ. Complexity science of multiscale materials via stochastic computations. *International Journal for Numerical Methods in Engineering* 2009; **80**(6):932–978.
93. Sakamoto S, Ghanem R. Polynomial chaos decomposition for the simulation of non-Gaussian nonstationary stochastic processes. *Journal for Engineering Mechanics* 2002; **128**(2):190–201.
94. Schweizer B, Wolff EF. On nonparametric measures of dependence for random variables. *The Annals of Statistics* 1981; **9**(4):879–885.
95. Fisher NI. Copulas. *Encyclopedia of Statistical Sciences*. Wiley: New York, 1997.
96. Noh Y, Choi KK, Liu D. Reliability-based design optimization of problems with correlated input variables using a Gaussian Copula. *Structural and Multidisciplinary Optimization* 2009; **38**(1):1–16.
97. Greene MS, Liu Y, Chen W, Liu WK. Stochastic multiscale analysis for complex material systems. *Tenth US National Congress on Computational Mechanics*, Columbus, OH, 2009.
98. Qian D, Wagner GJ, Liu WK, Yu MF, Ruoff RS. Mechanics of carbon nanotubes. *Applied Mechanics Reviews* 2002; **55**(6):495–533.
99. Pask JE, Sterne PA. Finite element methods in *ab initio* electronic structure calculations. *Modeling and Simulation in Materials Sciences and Engineering* 2005; **13**:R71–R96.
100. Beck TL. Real-space mesh techniques in density-functional theory. *Reviews of Modern Physics* 2000; **72**(4):1041–1080.
101. Sukumar N, Pask JE. Classical and enriched finite element formulations for Bloch-periodic boundary conditions. *International Journal for Numerical Methods in Engineering* 2009; **77**(8):1121–1138.
102. Abraham FF, Broughton JQ, Bernstein N, Kaxiras E. Spanning the continuum to quantum length scales in a dynamic simulation of brittle fracture. *Europhysics Letters* 1998; **44**(6):783–787.
103. Nakano A, Bachlechner ME, Kalia RK, Lidorikis E, Vashishta P, Voyiadjis GZ, Campbell TJ, Ogata S, Shimojo F. Multiscale simulation of nanosystems. *Computing in Science and Engineering* 2001; **3**(4):56–66.
104. Rafii-Tabar H, Hua L, Cross M. Multiscale numerical modelling of crack propagation in two-dimensional metal plate. *Materials Science and Technology* 1998; **14**(6):544–548.
105. Rafii-Tabar H, Hua L, Cross M. A multi-scale atomistic-continuum modelling of crack propagation in a two-dimensional macroscopic plate. *Journal of Physics—Condensed Matter* 1998; **10**(11):2375–2387.
106. Rudd RE, Broughton JQ. Coarse-grained molecular dynamics and the atomic limit of finite elements. *Physical Review B* 1998; **58**(10):R5893–R5896.
107. Rudd RE, Broughton JQ. Concurrent coupling of length scales in solid state systems. *Physica Status Solidi B—Basic Research* 2000; **217**(1):251–291.
108. Gavini V, Bhattacharya K, Ortiz M. Quasi-continuum orbital-free density-functional theory: a route to multi-million atom non-periodic DFT calculation. *Journal of the Mechanics and Physics of Solids* 2007; **55**(4):697–718.
109. Gavini V, Knap J, Bhattacharya K, Ortiz M. Non-periodic finite-element formulation of orbital-free density functional theory. *Journal of the Mechanics and Physics of Solids* 2007; **55**(4):669–696.
110. Gavini V, Bhattacharya K, Ortiz M. Vacancy clustering and prismatic dislocation loop formation in aluminum. *Physical Review B* 2007; **76**(18).
111. Hung L, Carter EA. Accurate simulations of metals at the mesoscale: explicit treatment of 1 million atoms with quantum mechanics. *Chemical Physics Letters* 2009; **475**(4–6):163–170.
112. Peng Q, Zhang X, Hung L, Carter EA, Lu G. Quantum simulation of materials at micron scales and beyond. *Physical Review B* 2008; **78**(5):054118.
113. Tadmor EB, Smith GS, Bernstein N, Kaxiras E. Mixed finite element and atomistic formulation for complex crystals. *Physical Review B* 1999; **59**(1):235–245.

114. Zhang P, Huang Y, Geubelle PH, Klein P, Hwang KC. The elastic modulus of single-wall carbon nanotubes: a continuum analysis incorporating interatomic potentials. *International Journal of Solids and Structures* 2002; **39**(13–14):3893–3906.
115. Liu B, Jiang H, Johnson HT, Huang Y. The influence of mechanical deformation on the electrical properties of single wall carbon nanotubes. *Journal of the Mechanics and Physics of Solids* 2004; **52**(1):1–26.
116. Johnson HT, Liu B, Huang Y. Electron transport in deformed carbon nanotubes. *Journal of Engineering Materials and Technology* 2004; **126**:222–229.
117. Bloch F. Über die Quantenmechanik der Elektronen in Kristallgittern. *Zeitschrift für Physik* 1928; **52**:555–600.
118. Kittel C. *Introduction to Solid State Physics*. Wiley: New York, London, Sydney, 1966.
119. Feynman RP. Forces in molecules. *Physical Review* 1939; **56**:340–343.
120. Li SF, Liu WK. *Meshfree Particle Methods*. Springer: Berlin, 2004.
121. Buttiker M, Imry Y, Landauer R, Pinhas S. Generalized many-channel conductance formula with application to small rings. *Physical Review B* 1985; **31**(10):6207–6215.